HHS Public Access

Differentiated daughter cells regulate stem cell proliferation and fate through intra-tissue tension

Wenxiu Ning[1], **Andrew Muroyama**[1,2], **Hua Li**[3], **Terry Lechler**[1,*]

[1]Departments of Dermatology and Cell Biology, Duke University Medical Center

[2]Present Address - Department of Biology, Stanford University

[3]Department of Pharmaceutical Sciences, Biomanufacturing Research Institute & Technology Enterprise, North Carolina Central University

SUMMARY

Basal stem cells fuel development, homeostasis, and regeneration of the epidermis. The proliferation and fate decisions of these cells are highly regulated by their microenvironment, including the basement membrane and underlying mesenchymal cells. Basal progenitors give rise to differentiated progeny that generate the epidermal barrier. Here, we present data that differentiated progeny also regulate the proliferation, differentiation, and migration of basal progenitor cells. Using two distinct mouse lines, we found that increasing contractility of differentiated cells resulted in non-cell autonomous hyperproliferation of stem cells and prevented their commitment to a hair follicle lineage. Increased contractility of differentiated cells resulted in impaired movement of basal progenitors during hair placode morphogenesis, and diminished migration of melanoblasts. These data suggest that intra-tissue tension regulates stem cell proliferation, fate decisions and migration, and that differentiated epidermal keratinocytes are a component of the stem cell niche that regulates development and homeostasis of the skin.

Graphical Abstract

*Lead Contact/Corresponding Author: Terry Lechler, Depts. of Dermatology and Cell Biology, Duke University Medical Center, 310 Nanaline Duke Bldg, Box 3709, Durham, NC, 27710, USA, Phone: 919 684-4550, terry.lechler@duke.edu.
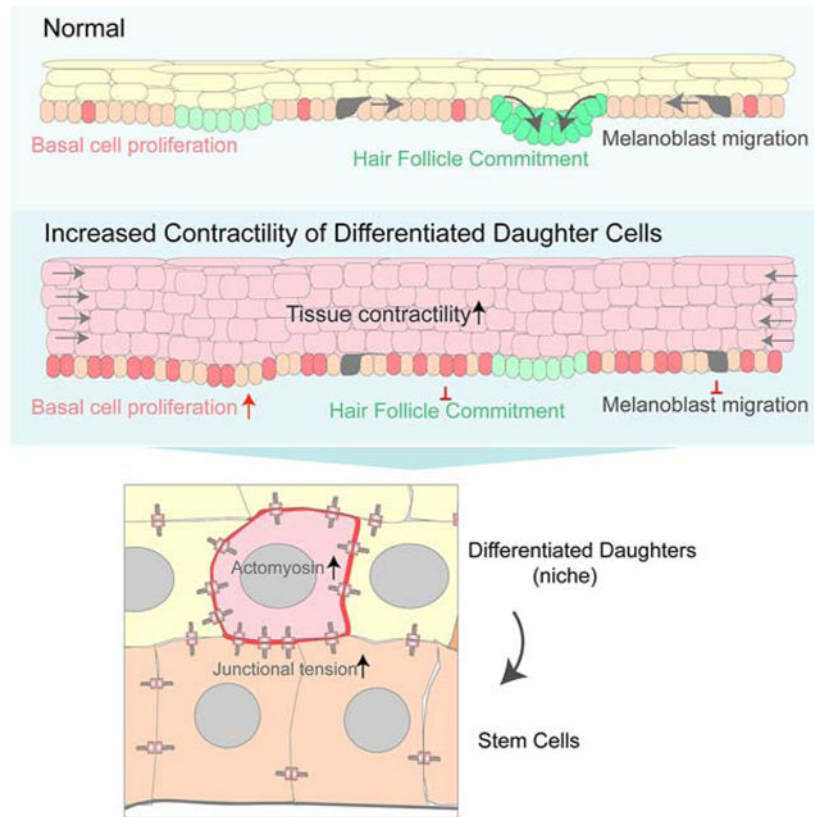
INTRODUCTION

Stem/progenitor cells drive the development, homeostasis and wound-healing of many tissues (Fuchs et al., 2004). In the skin, these progenitors lie in the basal layer of the epidermis, where they make contact with an underlying basement membrane that separates them from the underlying dermis (Figure 1A). During skin development and homeostasis, the basal stem cells proliferate and differentiate to generate suprabasal cells, thus maintaining a functional barrier. In addition, during embryonic development and wound-healing, basal cells migrate to form hair follicles or to heal cuts (Cetera et al., 2018; Ito et al., 2005; Ito et al., 2007). Understanding how stem cell fates and behaviors are determined by cues from their local microenvironment, termed the niche, is a fundamental goal to control and exploit stem cell activity.

Niche factors in the epidermis include signals from the underlying dermis (Goldstein and Horsley, 2012; Hsu et al., 2014; Watt and Fujiwara, 2011). There are important roles for factors secreted from mesenchymal cells, including dermal fibroblasts, adipose cells, vasculature, neurons, immune cells and lymphatics, in regulating the behavior of stem cells in the skin (Ali et al., 2017; Chen et al., 2012; Festa et al., 2011; Gur-Cohen et al., 2019; Hsu et al., 2014; Sharp et al., 2005). Notably, basement membrane attachment and the rigidity of the underlying substrate play regulatory roles in stem cell proliferation (Fuchs and Raghavan, 2002; Watt and Huck, 2013). Basal stem cells adhere to the extracellular matrix (ECM) through integrins which maintain proliferation and prevent differentiation of

epidermal progenitors(Adams and Watt, 1990; Grose et al., 2002; Jones et al., 1995; Raghavan et al., 2000; Watt, 2002). Stem cells are also sensitive to the rigidity of the basement membrane and underlying dermis. Increased rigidity promotes the proliferation of basal stem cells, presumably through integrin sensing and mechanotransduction (Discher et al., 2005; Handorf et al., 2015; Kechagia et al., 2019; Klein et al., 2009; Samuel et al., 2011; Wang et al., 2012). Another possible niche signal is from the progeny of the stem cells. These differentiated daughters remain in physical contact with their stem cells, and are ideally positioned to directly regulate them.

Paracrine signaling roles for differentiated daughters in controlling stem cell behavior have begun to be elucidated in other tissues (Hsu and Fuchs, 2012; Tata and Rajagopal, 2016). In the *Drosophila* midgut, daughter enteroendocrine cells regulate Notch signaling in adjacent stem cells to prevent their differentiation, and enterocyte death causes tissue damage and compensatory increases in stem cell proliferation (Amcheslavsky et al., 2009; Guo and Ohlstein, 2015; Jiang et al., 2009; Liang et al., 2017). In the fly hematopoietic system, progeny release factors that maintain stem cell quiescence (Mondal et al., 2011). In the lung, injury induces expression of BMP antagonists, promoting proliferation of stem cells (Tadokoro et al., 2016). Unlike these tissues, the skin epidermis is stratified (Figure 1A). The cell layers are attached to each other by cell-cell adhesion structures, allowing for direct cell-cell communication. Therefore, they have the potential for both paracrine and direct mechanical signaling in both directions. However, niche functions of differentiated cells, and their mechanical coupling to the basal progenitor have not been directly addressed.

Previously, we developed mouse lines to allow inducible gene expression in the differentiated cells of the epidermis (Muroyama and Lechler, 2017). Notably, we found that disruption of microtubules in these cells resulted in dramatic thickening of this tissue (Muroyama and Lechler, 2017). This was due to both cell-autonomous effects on cell shape in the differentiated cells and a non-cell autonomous increase in stem cell proliferation (Muroyama and Lechler, 2017). Here, we show that microtubule disruption results in increased actomyosin contractility which is both necessary and sufficient to induce stem cell hyperproliferation. Increased contractility also alters cell fates, inhibiting cells from fully committing to hair follicles. These effects are mediated, in part, by a cell migration defect due to increased contractility of overlying cells. Melanoblasts, which also migrate among basal progenitor cells, have similar defects in their migration. Our data demonstrate an increase in cell-cell adhesion stability, which likely underlies these effects. Therefore, we propose that stem cells of stratified tissues not only respond to substrate rigidity through integrin signaling, but also to intra-tissue tension. Further, this work establishes that the mechanical state of the differentiated cells is a niche signal that regulates multiple aspects of stem cell behavior.

RESULTS

Microtubule disruption results in increased cortical actomyosin

We previously showed that we could efficiently disassemble microtubules in differentiated epidermis by driving expression of an active form of the microtubule severing protein, spastin (K10-rtTA;TRE-HA-spastin, hereafter referred to as K10-Spastin) (Muroyama and

Lechler, 2017). Microtubule depolymerization in differentiated suprabasal cells of the epidermis leads to hyperproliferation of basal stem/progenitor cells (Figures 1B–1D, and 3F). While there was widespread expression of HA-Spastin throughout the differentiated layers of the epidermis, we observed expression in <1 or <3% of basal cells, from embryos and adults, respectively. Additionally, expression of Spastin in basal stem cells resulted in mitotic defects and delamination (Muroyama and Lechler, 2017), arguing that basal-cell hyperproliferation was likely driven by the non-cell autonomous defects in suprabasal cells. The hyperproliferative response occurred during both development and adulthood (Figures 1B–1D).

To explore the underlying mechanism of how differentiated cells regulate skin development and stem cell proliferation, we isolated keratin 10-positive differentiated cells from control and K10-Spastin embryos. Cells were sorted based on the expression of H2B-GFP, driven by K10-rtTA. Embryos were treated with doxycycline at e14.5 to induce spastin and H2B-GFP expression, then collected and FACS sorted for the GFP+ suprabasal cells at e16.5 (Figures S1A,B). Gene ontology (GO) term analysis of the resulting RNA-Seq dataset showed changes in signatures for epidermal development, peptide crosslinking, and lipid catabolism (Figure S1E). These are late epidermal differentiation signatures, consistent with our finding of premature barrier formation in K10-Spastin mice (Muroyama and Lechler, 2017). GO term and gene set enrichment analysis (GSEA) also revealed changes in actin cytoskeleton genes and in regulators of Rho-GTPase signaling (Figures 1E,F, S1C,D). As the actin cytoskeleton is a major determinant of cell shape, this offered a potential explanation for the cell-autonomous changes in cell morphology in these mice. Further, we noted that many of the significant changes were in genes associated with actomyosin contractility. The "contractome" contains just over 100 proteins that regulate actomyosin contractility (Zaidel-Bar et al., 2015), and we found that about 50% of these genes were differentially expressed in differentiated cells upon microtubule disruption, including myosin IIC and the upstream factors ROCK2, RhoC and ARHGEF2 (Figure S1C). Thus, our RNA-Seq analysis suggested that microtubule disruption in differentiated cells might alter F-actin organization and contractility.

To validate these findings, we first stained actin filaments. Quantification of the intensity across intercellular junctions of the microtubule-disrupted cells showed a dramatic increase in cortical F-actin (Figures 1G and 1H). Notably, F-actin levels between non-spastin-expressing basal cells and spastin-expressing spinous cells in K10-Spastin were also higher than in controls, demonstrating changes at this important interface (Figures 1I and S1F). Non-muscle myosin II molecules assemble into bipolar filaments and bind to F-actin to generate contractile forces (Vicente-Manzanares et al., 2009). Myosin IIC, which showed an approximately 12 fold increase at the mRNA level, also showed an increase at the protein level by western blot (Figure S1G). It was highly enriched at the cortex of the differentiated cells in K10-Spastin embryos (Figures 1J,K). In contrast, myosin IIA and IIB were not significantly altered in the mutant epidermis (Figures S1H,I). These data indicate that microtubule depolymerization can increase cortical actomyosin contractility in suprabasal differentiated cells of the skin epidermis. To determine the effects of spastin expression and upregulation of cortical actomyosin on tissue mechanics, we obtained full thickness skin explants of control and K10-Spastin skin and cultured them for 24 hours with doxycycline.

Consistent with increased contractility, the K10-Spastin skin showed a notable decrease in area over time (Figures 1L,M).

Microtubule disruption stabilizes adherens junctions.

Cortical actomyosin complexes can interact with and productively engage adherens junctions. Adherens junctions are mechanosensitive and responsive structures that can be stabilized by the external application of force (le Duc et al., 2010; Yonemura et al., 2010). Since cortical actomyosin was increased in microtubule-disrupted suprabasal cells, we asked whether the increased cortical actomyosin altered adherens junctions *in vivo*. We stained with the α−18 antibody, which recognizes an epitope of α-catenin that is exposed when junctions are under tension (Yonemura et al., 2010). While there was not a significant change in the levels of total α-catenin at the cell cortex (Figures 2A,E), cortical α−18 levels between spinous cells were increased in K10-Spastin as compared to control skin (Figures 2A,C). This was also true at the junction between stem cells and their differentiated progeny (Figure 2D).

Vinculin also often marks adherens junctions under increased tension (Yonemura et al., 2010). Consistent with the increase in cortical α−18 signal, we observed increased cortical intensity of vinculin in microtubule-disrupted cells (Figures 2B,F). Another readout of contractility in many cell types is the mechano-responsive transcriptional co-activator YAP/TAZ. This protein is nuclear in many embryonic basal progenitors, where it plays an important role in driving proliferation (Zhang et al., 2011). In differentiated cells of control epidermis, YAP was cytoplasmic or not detectable. However, there was a clear nuclear YAP signal in the differentiated epidermis of K10-Spastin embryos (Figure S2A,B). As most basal progenitors in the embryo are YAP positive in control mice, there was not a clear increase in the mutant. However, in the adult skin, YAP-positive basal cells are rare in control epidermis, while they were increased in the K10-Spastin mutant (Figures S2C–S2F). Together, these data demonstrate that microtubule depolymerization increases actomyosin contractility and adherens junction engagement.

Increased junctional tension can alter the stability and/or turnover of E-cadherin complexes (Rao and Zaidel-Bar, 2016; Verma et al., 2012). To examine this, we used E-cadherin-CFP mice crossed to control or K10-Spastin. This is a fully functional E-cadherin tagged at its endogenous chromosomal locus (Snippert et al., 2010). Fluorescence recovery after photobleaching (FRAP) experiments were performed on skin explants. In normal epidermis, E-cadherin-CFP recovered to about 36% of its initial intensity within 200 seconds. In K10-Spastin epidermis, the recovery was only 15% (Figures 2G, and 2H). These data demonstrate that the increased actomyosin contractility induced by microtubule disruption not only leads to changes consistent with increased junctional tension but also to stabilization of cortical E-cadherin complexes.

Contractility is required for both cell autonomous and non-cell autonomous effects of microtubule disruption

While contractility was increased in spastin-expressing cells, it was unclear whether it was required to drive the cell autonomous effects and/or the non-cell autonomous effects caused

by microtubule depolymerization. We thus treated embryos with two different inhibitors of contractility to determine whether this could rescue the phenotypes. Non-muscle myosins were targeted with blebbistatin (Kovacs et al., 2004), while the upstream regulator, ROCK1/2, was inhibited with Y-27632 (Pellegrin and Mellor, 2007). We injected pregnant dams with these inhibitors to decrease myosin activity (Figure S3D). Decreasing contractility with either inhibitor rescued the skin thickness as well as cell aspect ratio compared to untreated K10-Spastin embryos (Figures 3A–3E). Cell aspect ratio was not completely rescued, and it remains unclear whether this is because of incomplete inhibition or whether microtubules play a more direct role in cell shape control (Figure 3D). Remarkably, decreasing contractility rescued basal cell proliferation in the K10-Spastin epidermis. The inhibitors did not have a significant effect on proliferation in control epidermis (Figures 3F, and S3A–C). The intensity of α18 at spinous cell junctions was decreased by both of the inhibitors, demonstrating effects consistent with lowering of junctional tension (Figures 3G,H).

Contractility of differentiated daughters is sufficient to induce stem cell proliferation

The above data demonstrate that contractility of differentiated cells is necessary to induce progenitor cell proliferation, but does not address whether it is sufficient. To test a direct role for suprabasal cell contractility in regulating basal stem cells, we developed a mouse line that inducibly increases contractility using a constitutively active Rho-GEF (TRE-HA-Arhgef11^{CA}) to increase actomyosin contractility without disrupting microtubules. Arhgef11 is a PDZ-domain-containing Rho guanine nucleotide exchange factor (RhoGEF) that binds and activates RhoA through its catalytic DH-PH domains (Valon et al., 2017) (Figure 4A). Addition of a membrane targeting domain enforced membrane localization. Transfection of this construct with K14-rtTA into cultured keratinocytes revealed membrane localization of Arhgef11^{CA} and cell rounding with increased cortical F-actin (Figure S4A). Notably, neighbor cells were elongated toward the contracting Arhgef11^{CA} cells, consistent with increased contractility.

We established a mouse line K10rtTA; TRE-Arhgef11^{CA} (hereafter referred to as K10-Arhgef11) that allows doxycycline-inducible Arhgef11^{CA} expression in suprabasal cells, and found a similar cortical localization in the differentiated cells *in vivo* as we observed in cultured keratinocytes *in vitro* (Figures 4A,B). As with K10-Spastin, there was no basal expression in the embryo, and in the adult, only <5% of basal cells were labeled. K10-Arhgef11^{CA} mice had thick flaky skin, lacked external ears, and had misshapen paws and curly tails (Figure S4C). These mice had the same premature barrier acquisition phenotype and impaired corneocyte morphology as observed in K10-Spastin mice (Figures 4C and S4D). There was a clear increase in tissue contractility when Arhgef11^{CA} was induced in *ex vivo* cultured skin, resulting in shrinkage of skin explants over time (Figure S4B).

These similarities were also reflected at the cell and tissue levels. K10-Arhgef11 embryos had a thickened epidermis and decreased aspect ratios of spinous and granular cells (Figures S4E–S4G). Similar to K10-Spastin, we noted a decrease in cortical intensity of desmosome components in K10-Arhgef11 skin, demonstrating that increased contractility leads to desmosome down-regulation (Figures S4K,L).

Importantly, there was also increased proliferation of basal stem cells in the K10-Arhgef11 mice in both embryos and adults (Figures 4E and S4I). Increased proliferation was first noted 24 hours after induction of Arhgef11. We first detected transgene expression (mosaicly) at 6h after induction (Figure S4H), while increased cortical F-actin was first evident at 12h post-induction (Figure 4F, embryo; and Figure S4J, adult). In further support of the non-autonomous nature of this hyperproliferation, we found that induction of Arhgef11^{CA} in basal stem cells (using Krt14-rtTA) resulted in hypoproliferation, not the hyperproliferation induced by contractility of differentiated cells (Figure S4M). Similar to K10-Spastin, nuclear YAP was also increased in the K10-Arhgef11 mice (Figures S2E,F), and the hyperproliferation phenotype in the adult skin of K10-Arhgef11 mice was also partially rescued by contractility inhibitors, as well as by the YAP inhibitor, verteporfin (Figures 4G–4I).

Arhgef11^{CA} expression increased cortical α−18 staining intensity both between spinous cells and at the basal/spinous interface (Figures 4J,K), reflecting the increased junctional tension across this interface. To confirm whether junctional stability was increased by the Arhgef11^{CA}-expressing tissue, we performed FRAP analysis of E-cadherin-CFP in these embryos. This revealed a similar level of adhesion strengthening as was observed in spastin-expressing embryos (Figures 4L, 4M, 2G and 2H). Together, these data demonstrate that increased contractility of differentiated cells is both necessary and sufficient to induce stem cell proliferation.

To determine the spatial localization of contractility that is required to promote stem cell proliferation, we turned to another driver line, Involucrin-tTA, that allows doxycycline to repress expression from the TRE promoter (i.e. a tet-off system, in contrast to the tet-on provided by rtTA) in upper spinous and granular cells of the epidermis but not in immediate suprabasal cells (Jaubert et al., 2004a) (Figure S5A). In combination with the TRE-Arhgef11 allele, we found mosaic expression throughout the epidermis at different developmental stages. At E16.5, Arhgef11^{CA} expression was largely restricted to the upper spinous and granular layers. However, in some focal areas it was found even in the spinous cells immediately adjacent to the basal progenitors (Figures S5A,B). We found that areas with increasing numbers of adjacent cells expressing Arhgef11^{CA} showed increasing levels of basal progenitor cell proliferation (Figures S5B–S5D). These data are consistent with direct cell-cell contact being required between the contractile cell and the basal progenitor, and are inconsistent with this signal being transmitted across multiple cells or systemically.

Contractility causes non-cell autonomous defects in hair follicle formation

During skin development, the epidermal stem cells in the basal layer undergo fate decisions. They either differentiate and move up into stratified interfollicular epidermis or invaginate and migrate towards the dermis to generate hair follicles. When we induced spastin expression at E16.5, the resulting pups had less hair (Figures 5A,B). To understand whether hair follicle development could be affected by the increased actomyosin contractility of Krt10+ suprabasal cells, we induced expression of spastin or Arhgef11^{CA} at E14.5 and analyzed hair follicles at later stages. Lhx2, a transcription factor that is expressed in hair follicles beginning at the late placode stage, was used to quantitate hair follicle number.

There was a clear decline in hair follicles in both mouse models (Figures 5C–5F). In contrast, in Inv-Arhgef11 mice we observed that hair follicles still formed in regions where Arhgef11[CA] expression was largely limited to granular cells (Figures S5E,F). These data demonstrate that the hair follicle defect depends on close contact of contractile cells.

To begin to determine the temporal window in which contractility works, we also induced expression at later time points, E16.5 and E18.5, and examined effects at postnatal day zero (P0 - neonates) (Figures S6A–S6D). The later the treatment of doxycycline, the less severe the impact on hair follicle numbers in neonatal mice, suggesting that contractility likely acted early during hair follicle morphogenesis and did not significantly affect hair follicles once they had passed some threshold stage of development. As the first wave of hair placodes is already specified at E14.5, concomitant with the induction of expression of the spastin or Arhgef11[CA], these hair follicles are likely spared from their effects. That said, we cannot rule out that the guard hairs are less sensitive to these effects.

The hair follicle defects seen in K10-Spastin embryos were largely rescued by decreasing contractility with Y27632 and blebbistatin (Figures 5G,H). Consistently, directly increasing actomyosin contractility by expressing Arhgef11[CA] also decreased hair follicle specification (Figures 5E,F).

Hair follicle morphogenesis begins with the formation of a thickened epithelium, called a placode (Figure 6A). Wnt signaling is required for hair follicle specification (Andl et al., 2002), and Lef1 marks cells as they commit to the hair fate (note that it also marks underlying dermal condensate cells). Subsequently, additional regulators, first EDAR (Ectodysplasin receptor), and then Lhx2 are expressed. In the late hair placode, Lhx2 labels the basal cells, while Sox9+ marks a population of cells directly above them (Ouspenskaia et al., 2016). To verify that the phenotypes we observed were in fact non-cell autonomous, we examined the position of Krt10[+ve] cells relative to hair follicle placodes using K10-rtTA;TRE-H2B-GFP embryos. At the earliest stages of placode formation, H2B-GFP was expressed in cells overlying the forming placode, but not in the cells that are committing to a placode fate (Figure S6I). At slightly later stages, a suprabasal layer of placode cells forms and contains a population of cells that are Sox9[+ve]. These cells did not express H2B-GFP and we never detected spastin or Arhgef11[CA] in these cells (Figure S6J). This indicates that the hair follicle specification defects in these two mouse models resulted from non-cell autonomous effects on actomyosin contractility in overlying differentiated cells. This is striking as it demonstrates that suprabasal cells can regulate basal stem cell fate during hair follicle specification.

Contractility affects placode progression but not specification

Hair placode specification is initiated by Wnt/β-catenin signaling, which is required for subsequent EDAR expression (Fu and Hsu, 2013; Zhang et al., 2009). EDAR/NF-κB signaling is required to maintain and refine the pattern of Wnt/β-catenin activity at later stages of placode development (Zhang et al., 2009). Meanwhile, NF-κB directly targets *LHX2*, which is required for the subsequent down-growth of the hair placode (Tomann et al., 2016). In this study, we define Lef1, Edar, and Lhx2 expression as marking early, mid, and late placode stages, respectively (Figures 6A,B and S6E–G). Consistently, the number of

Lhx2^{+ve} placodes, as well as the number of dermal condensates (marked by Sox2), was decreased when microtubules were disrupted in differentiated cells (Figures 6C and 6E).

To further explore earlier stages of hair placode formation, we stained for EDAR. The number of EDAR^{+ve} placodes was also lower in K10-Spastin embryos compared to controls (Figures 6F,G and S6H). We next stained for Lef1, the earliest marker of commitment to a hair follicle fate. This analysis was performed on whole-mount epidermis, which gives a clearer view of placode coalescence. The number of Lhx2^{+ve} placodes was decreased in K10-Spastin epidermis (Figures 6H,I), consistent with our findings in tissue sections. In control epidermis, early placodes were marked by Lef1 and were not highly condensed. Later stage placodes were morphologically distinct, being tightly packed with clear boundaries (Figure 6M). The total number of Lef1 patches was similar in the control and K10-Spastin mutant epidermis, demonstrating that initial hair follicle specification is not affected. However, the placodes in the K10-Spastin epidermis were mostly of the early/ diffuse sort, with few of the more advanced placodes (Figures 6J,K). The Lef1^{+ve} placodes contained similar numbers of cells in the control and mutant skin, demonstrating that subsequent defects were not due to a change in placode cell number (Figure 6L). Therefore, suprabasal contractility regulates hair follicle fate downstream of their specification and is required for both morphological and gene expression changes (Figure 6M). Together, these data demonstrate that differentiated suprabasal cells not only regulate basal stem cell proliferation but also their cell fate during hair placode morphogenesis.

Contractility decreases cell migration of placodal cells and melanoblasts

Prior work suggested cell migration drives placode coalescence during hair follicle initiation (Ahtiainen et al., 2014; Cetera et al., 2018). We thus turned to live imaging of placode formation in skin explants to determine whether there were changes in cell dynamics in the K10-Spastin embryos. Using a membrane-bound GFP reporter, we observed placode cell dynamics in control and K10-Spastin embryos. In control embryos we found that early placodes underwent a consistent change in morphology, acquiring a smaller diameter over time. This change was not observed in the mutant skin (Figures 7A,B). When quantitated by blinded observers, approximately 80% of placodes progressed in control skin, while less than 20% did in the mutant skin (Figure 7C). We next tracked cell movements within the placode by labeling them with a K14-Cre; Rosa-LSL-H2B-mCherry reporter. Individual cell tracks were consistently shorter in the mutant as compared to the wild-type tissue (Figure 7D). Collectively, the live imaging results suggest that actomyosin contractility in differentiated suprabasal cells controls progenitor cell fates by regulating their cell migration during hair placode morphogenesis.

The embryonic epidermis consists not only of epidermal stem cells and their descendants but also melanoblasts. Melanoblasts are neural-crest derived cells that invade into the epidermis at E12.5 and migrate quickly through the basal layer of progenitor cells, eventually homing to hair follicles in the mouse (Mort et al., 2015). In tissue sections, staining of the melanoblast marker c-kit in the control epidermis demonstrated that the majority of melanoblasts sit within the basal layer of the epidermis, forming protrusions that traverse through lateral junctions, just above the basement membrane, and at the interface between

suprabasal cells and basal cells (Figures 7H and S7D). To determine whether the effects of increased suprabasal contractility were unique to the keratinocyte lineage, we imaged the movement of melanoblasts labeled with Tyr-Cre; Rosa mT/mG (Figure 7E). Melanoblasts migrated at an average speed of ~0.23 μm per minute in the control epidermis, and this was decreased to ~0.11 μm per minute in K10-Spastin embryos (Figures 7E,F). Melanoblasts exhibited very dynamic protrusions from the cell body. Large protrusions were conduits through which the cell body would move (Figure 7G). While K10-Spastin mice formed protrusions normally, the translocation of the cell body through these protrusions was rare (Figure 7G). While melanoblasts in K10-Spastin embryos had normal numbers of protrusions, there was a slight increase in the length of the leading process, likely due to the lack of cell body movement into them (Figures S7B and S7C). Because junctional remodeling is required for motility, the diminished migration observed in K10-Spastin likely results from adhesion strengthening induced by increased contractility.

Consistent with high expression of E-cadherin in migrating melanoblasts (Mort et al., 2015), co-staining of E-cadherin with the melanoblast marker c-kit showed that melanoblasts form contacts with both basal and suprabasal keratinocytes, and have protrusions at the interface between basal and suprabasal layers (Figures 7H and S7D). Therefore, the melanoblast migration defects may result from direct effects on stabilized junctions between melanoblasts and keratinocytes or between cells through which they are traversing.

In summary, these data demonstrate that differentiated epidermal cells play broad and unexpected roles in the skin. In addition to their role in generating a physiological barrier, they regulate the proliferation and fate decisions of underlying basal stem cells, as well as the migration of melanoblasts.

Discussion

In this work, we demonstrated that the differentiated cells of the epidermis can regulate proliferation, migration and cell fate decisions of the underlying stem cells from which they are derived. Further, our evidence demonstrates that the contractility of these cells is key in determining stem cell behavior by both promoting proliferation and inhibiting migration.

A key finding in this work is that loss of microtubules results in increased cell contractility. Microtubule-actin crosstalk is mediated through both direct coupling by cross-linkers and by indirect signaling mechanisms controlled by Rho GTPases and their regulating GEFs and GAPs (Dogterom and Koenderink, 2019; Rodriguez et al., 2003). In some other cell types, Arhgef2/GEF-H1, which is an activator for the contractility-inducing RhoA GTPase, can mediate this effect. This GEF has low activity when bound to microtubules, and that activity increases when microtubules are disrupted (Krendel et al., 2002; Nagae et al., 2013). However, we also saw a transcriptional upregulation of contractome genes. Therefore, it will be important to determine what mediates the transcriptional response and whether it is directly responsible for the contractility or a feedback mechanism that amplifies it. Further understanding of the mechanism will also inform how sensitive this response is to changes in microtubule dynamics and/or organization.

There are a number of ways in which contractility could regulate stem cell behavior. Effects could be indirect; contractility in differentiated cells may alter their secretome or cell surface composition, thus resulting in local or systemic changes (Figure S7E). As the proliferation changes described here occurred locally, we can rule out systemic signaling. It is more difficult to determine the effects of changes to paracrine factors or direct contact of signaling molecules. An intriguing possibility is that contractility acts via mechanical signaling to alter the behavior of underlying stem cells (Figure S7E). In support of this, we show that increased contractility results in changes in the dynamics of E-cadherin, a major transmembrane component of the adherens junctions in these cells. Effective migration of cells through the basal layer requires the making and breaking of cell contacts. Decreased turnover of adherens junction would limit the ability to productively change neighbors and thus move within the tissue. Second, the direct application of force on adherens junctions in cultured cells was sufficient to induce their proliferation through both Yap1 and β-catenin-dependent pathways (Benham-Pyle et al., 2015). A similar effect in the skin may underlie the ability of differentiated cells to communicate mechanically with the underlying progenitors. In support of this, we saw an increase in nuclear YAP-positive basal cells when contractility was increased in differentiated cells in the adult epidermis. Further, pharmacologic inhibition of YAP reduced contractility-induced proliferation. In contrast, we did not see an upregulation of Wnt target genes (data not shown). Effects on actin dynamics and adherens junction turnover on one side of a junction are usually associated with changes on the other side, so it is likely that basal cells sense the changes in their overlying progeny (Indra et al., 2020). In support of this, we found that the interface between stem cells and differentiated cells had higher levels of both F-actin and α18 staining, suggesting that basal cells can sense this change across their junctions. In contrast, decreasing contractility in the epidermis does not appear to have significant effects on stem cells (Chrostek et al., 2006; Jackson et al., 2011; Sumigray et al., 2012). Additionally, we previously demonstrated that loss of both myosin IIA and B in the epidermis did not cause profound changes in epidermal thickness, while other have noted slight decreases in interfollicular epidermal thickness upon knockout of myosin IIA in their genetic background (Le et al., 2016; Sumigray et al., 2012).

Epidermal stem cells sense and react to the mechanical signals from the niche, including the stiffness of the basement membrane/dermis. Unlike cell-ECM interactions, the role of intra-tissue contractility in regulating stem cell behavior has not been studied in detail. The data presented here is consistent with a similar mode of mechanosensation at adherens junctions that modified stem cell behavior.

Increasing contractility in differentiated cells had non-cell autonomous effects not only on basal cell proliferation but also on hair follicle formation. This defect stemmed from a defective migration of cells fated toward hair follicles. While the ultimate fate of these cells is unclear, we have not noted apoptotic bodies. One likely possibility is that, in the absence of tight clustering, the signals required to maintain their fates are lost and these cells revert into interfollicular stem cells. Motility defects were also found in melanoblasts which quickly migrate through the relatively static basal stem cells. Transient adherens junctions form between melanoblasts and keratinocytes, and adhesions must be remodeled to allow the melanoblast nucleus to move through. This finding provides an intriguing perspective to explore contributions of the interaction between melanocytes and keratinocytes during

metastatic melanoma formation. It also raises the question of whether the migration of other immune regulatory cells in the epidermis is affected by altered contractility of differentiated cells.

Finally, the work here has important implications for the analysis of gene function in stem cells. Traditional genetic methods to assign gene function in stem cells rely on tissue or cell-type specific recombination approaches. This obligately results in loss of gene function in the progeny of the stem cell, making it difficult to separate cell autonomous effects of gene function in stem cells from non-cell autonomous functions in their differentiated progeny. Therefore, new tools that are able to specifically cause changes in either basal progenitors or their progeny are required to precisely delineate pathways controlling epidermal regulation.

Limitations of this study.

While this study demonstrates that contractility of differentiated cells regulates the proliferation and migration of underlying stem cells, the mechanism underlying this influence has not been established. In addition, pharmacological inhibitors of contractility and Yap pathway activity were used. As we understand more about these pathways, genetic targeting to validate these findings will be required.

STAR METHODS

RESOURCE AVAILABILITY

Lead contact—Further information and requests for resources and reagents should be directed to and will be fulfilled by Dr. Terry Lechler (terry.lechler@duke.edu).

Materials Availability—This study generated new reagents and datasets that are available online (GEO: GSE158785) or are available from Dr. Lechler (TRE-Arhgef11 mice).

Data and Code Availability—The accession number for the scRNA-seq dataset reported in this paper is GEO: GSE158785. All other datasets and code are available upon request from the Lead Contact.

EXPERIMENTAL MODEL AND SUBJECT DETAILS

Mice—All animal work was approved by Duke University's Institutional Animal Care and Use Committee. All mice were maintained in a barrier facility with 12 hour light/dark cycles. Mouse strains used in this research were: K10-rtTA and TRE-Spastin mice were generated in the lab as previously described (Muroyama and Lechler, 2017). Involucrin-tTA mouse was previously described (Jaubert et al., 2004). All other mice were purchased from Jackson Laboratories, and their stock number is indicated. TRE-H2B-GFP (005104); Rosa-mT/mG (007576); mGFP were generated by mating Rosa-mT/mG mice with a CMV-Cre-deleter strain (006054); Tyr-Cre (029788); K14Cre (018964); Rosa26-LSL-H2B mCherry (023139); E-cadherin-CFP (016933). CD1 mice were purchased from Charles River (Strain code: 022).

Generation of the TRE-Arhgef11^{CA} mouse line:

Arhgef11^{CA} with a membrane targeting domain and an HA tag with a stop code on the C-terminal was synthesized by GenScript. NheI and Sal I sites were inserted on the 5' and 3' ends of the Arhgef11^{CA} cassette, respectively and used to clone into the pTRE2 vector. Doxycycline-dependent expression of the Arhgef11 cassette was first verified in cultured keratinocytes by co-transfecting with K14-rtTA plasmid. The Arhgef11^{CA} plasmid was linearized with AatII and BsaxI, purified and was used by the Duke Transgenic Core to generate transgenic TRE-Arhgef11^{CA} mice via pronuclear injection.

Inhibitor Experiments—For BrdU experiments, BrdU (10 mg/kg) was intraperitoneally injected into adult or pregnant dams (for embryos) one hour before sacrificed for tissue dissection and processing.

For drug rescue experiments in K10-Spastin, pregnant dams were fed with doxycycline chow starting at E14.5. They were intraperitoneally injected twice the next day (one early in the morning and one at night) with Y-27632 2HCl (Selleckchem, Cat. No. S1049) at 10 mg/kg per mouse, or with blebbistatin (Sigma, B0560) at 2 mg/kg per mouse.

For drug rescue experiments in adult, mice were injected with Y-27632 (10 mg/kg), blebbistatin (2 mg/kg), or verteporfin (VWR/US pharm conv, 1711461, 100mg/kg) at 12 hrs after doxycycline chow, BrdU injected and sacrificed after 24 hrs doxycycline chow.

Cells and transfection—Stable wildtype keratinocytes established from primary mouse keratinoyctes were maintained in E low Ca^{2+} medium at 37°C and 7.5% CO$_2$. Plasmids of K14-rtTA and pTRE2-Arhgef11^{CA} were co-transfected into keratinocytes using Mirus transfection reagents (Mirus). 12 hours after infection, cells were switched to E high Ca^{2+} medium (1.2 mM Ca$^{2+)}$ to induce differentiation and with doxycycline (2 μg/ml) to induce Arhgef11^{CA} expression.

Skin explant culture—Embryos at E15.5 were sacrificed, then rinsed and placed in sterile PBS. Back skin was cut off, rinsed, and gently unfolded in sterile PBS, then placed on an agarose pad (4% agarose in sterile water mixed 1:1 with 10%FBS in DMEM (Gibco, Cat. No.11965), and with doxycyline (2 μg/ml), and 1:100 Penicillin/Streptomycin (Gibco, Cat. No.10378016)). Skin explants on agarose were gently placed into a 6 cm dish containing 1ml 10% FBS in Gibco-DMEM (to avoid agarose drying), and were cultured at 37°C and 7.5% CO$_2$ for at least 2 hours for recovery before live imaging.

METHOD DETAILS

RNA-Seq analysis—K10-rtTA;TRE-H2B-GFP;TRE-Spastin pregnant dams were fed with doxycycline chow at E14.5, then sacrificed at E16.5. Embryos were checked by dissecting microscope for GFP expression, tails were taken to confirm genotype, and back skins were cut off and treated with dispase II (1.4 U/ml) in HBSS at room temperature for 1 hour. The epidermis was then peeled off from the dermis, and digested in 1:1 trypsin (Gibco, Cat. No. 25200–056) with versene (Gibco, Cat. No. 15040–066) at 37°C and rotated for 20 minutes, then mixed 1:1 with FACS buffer (HBSS with 2.5% FBS and 10 μg/ml DNAaseI) and centrifuged. The cell pellet was diluted into FACS buffer with propidium iodide solution (Sigma P4864), filtered using sterile Celltrics 30 μm filters (04-004-2326, Sysmex), and

FACS sorted for GFP positive and PI negative cells. RNA was extracted using a Qiagen RNAeasy Mini kit (Qiagen, Cat No.74104) following the manufacturer's protocols, with DNA digested using RNase-Free DNase (Qiagen, Cat No.79254). Three independent RNA samples from control and K10-Spastin were collected and sent for sequencing and analysis by Novogene.

Differentially-expressed genes (p-value<0.01, FDR<0.05) by FPKM for certain pathway were centered, log2-transformed, and used to generate heatmaps. The complete differentially expressed genes (p-value<0.01, FDR<0.05, 2999 genes in total) were analyzed for the gene set enrichment using GSEA software (Subramanian et al., 2005) (guidelines from https://www.gsea-msigdb.org/gsea/index.jsp). GO term analysis for differentially expressed genes (fold-change>2 in K10-Spastin/control, p-value<0.01, FDR<0.05) was performed using WebGestalt (Wang et al., 2017) online resources (http://www.webgestalt.org/).

X-Gal barrier assay—E16.5 embryos were rinsed in PBS, then were placed into the staining solution (1 mg/ml X-gal, 1.3 mM $MgCl_2$, 100 mM NaH_2PO_4, 3 mM $K_3Fe[CN]_6$, 3 mM $K_4Fe(CN)_6$, 0.01% sodium-deoxycholate, 0.2% NP-40), incubated at 37°C until color developed, washed in PBS for 1–2 minutes and then photographed.

Cornified envelope preparations—Epidermis was isolated as above and then boiled for 10 minutes in 10 mM Tris (pH 7.4), 1% β-mercaptoethanol, and 1% SDS. Corneocytes were pelleted and resuspended in PBS and photographed.

Western blot—Skin epidermal samples were prepared as previous described (Sumigray et al., 2012). Epidermal proteins from control and K10-Spastin were solubilized in loading buffer (10% SDS, 40% Glycerol, 3% Bromophenyl Blue, and 10% β-mercaptoethanol), boiled for 10 minutes and loaded into 10% polyacrylamide gels and run for ~90 mins at 120V, then transferred onto nitrocellulose membrane, blocked with 5% BSA, and immunoblotted with primary antibodies for Myosin IIC (Biolegend, 919201) and GAPDH (Abcam, ab9485) overnight. Blots were washed three times in PBST (0.1% Tween in PBS), incubated with secondary antibodies (Licor, IRDye 680RD Series, CW800 Series), then visualized using a LI-COR Odyssey FC system.

Immunofluorescence analysis—Skin tissue sections were fixed with 4% PFA at room temperature for 10 minutes or with ice-cold acetone (for Myosin IIC and vinculin) for 2 minutes, washed in PBS containing 0.2% Triton X-100, then incubated with blocking buffer (3% BSA with 5% NGS and 5% NDS for most antibodies, NGS was absent when using goat antibodies and MOM block was used for mouse primary antibodies). Sections were incubated in primary antibody diluted in blocking buffer for 1h at room temperature (α−18 incubated for 15 minutes), then washed, and incubated in secondary antibodies and Hoechst for 1 hour, washed, and finally mounted in the anti-fade buffer (90% glycerol in PBS plus 2.5 mg/ml p-Phenylenediamine (Sigma-Aldrich)). For BrdU staining, sections were treated with pre-warmed 1N HCL at 37°C for 40 minutes after 4% PFA fixation, followed by immunofluorescence staining as above.

For whole mount immunofluorescence staining, back skins were dissected off of embryos and treated with dispase at room temperature for 1 hour, and then the epidermis was peeled off from the dermis and fixed with 4% PFA for 30 minutes at room temperature. Skins were then washed and incubated with blocking buffer for 1 hour, and incubated with diluted primary antibodies in blocking buffer at 4 °C overnight. The next day they were washed again and incubated with secondary antibodies and Hoechst for 2 hours at room temperature, then washed and imaged.

Primary antibodies used in this study: rab anti-HA (Abcam, ab9110), rat anti-HA (Sigma-Aldrich, 11867423001), chicken anti-keratin 5/14 (generated in the Lechler lab), rabbit anti-keratin 10 (Covance, 905401), rat anti-BrdU (Abcam, ab6326), rat anti-β4 integrin (BD Biosciences, 553745), MyosinIIA (Biolegend, PRB-440P), MyosinIIB (Biolegend, 909901), MyosinIIC (Biolegend, 919201), α-catenin (Sigma-Aldrich, C2081), α−18 (gift from Akira Nagafuchi), Vinculin (Sigma-Aldrich, V9131), YAP/TAZ (Cell Signaling Technology, 8418S), LHX2 (Santa Cruz, 19344), SOX9 (Millipore, Ab5535), EDAR (Novus Bio, AF745), LEF1 (Cell Signaling Tech, 2230), E-cadherin (BD, 610182), c-Kit (Cell Signaling Technology, 3074S), Desmoglein 1 (BD, 610273), Desmoplakin (Chemicon/Millipore, CBL173). F-actin was stained with phalloidin (Invitrogen, A12379 and Sigma-Aldrich, P1951).

Imaging—For section and whole mount staining, slides were imaged on a Zeiss AxioImager Z1 microscope with Apotome.2 attachment, Plan-APOCHROMAT 20X/0.8 objective, Plan-NEOFLUAR 40X/1.3 oil objective, or Plan-NEOFLUAR 63X/1.4 oil objective, Axiocam 506 mono camera, and acquired using Zen software (Zeiss).

For live-imaging of hair placode and melanoblast migration, skin explants were placed upside down in a Lumox dish 35 (94.6077.331, Sarstedt), with epidermal side facing toward the membrane. Images were acquired on an Andor XD revolution spinning disc confocal microscope at 37°C and 5% CO_2 using a 20x/0.5 UplanFl N dry objective, and were acquired using MetaMorph software. Images were taken at 15 min intervals for placode imaging and at 10 min intervals for melanoblast imaging.

For FRAP assay of E-cadherin-CFP, skin explants were placed upside down on glass-bottom dishes (MatTek, P35G-1.5–14-C), with epidermis side facing toward the glass-bottom. FRAP assays were performed within one hour of mounting for each sample, using Leica SP5 Inverted Confocal microscope with 100x/1.4–0.70 oil objective, and was acquired using Leica confocal LAS AF software by setting up bleaching regions across junction, and taking time series before and after photobleaching.

Image quantification and Statistics—All images quantifications were done using FIJI software. Quantifications of fluorescence intensity of cortical F-actin, Myosin IIC, α-catenin, α−18, desmoplakin, and desmoglein 1 were measured by drawing lines across cell-cell boundaries, and analyzed for their plot profiles, maxima were aligned and the ends were trimmed to yield the final line scan. Quantification of BrdU+ basal cells were performed by measuring numbers of BrdU+ cells and total basal cells for each field, and calculating the mean percentage of all fields for each mouse. Aspect ratios for granular and spinous cells

were calculated by tracing individual cells and using the measurement option in FIJI to measure cell length and width. For recovery rate of E-cadherin-CFP, intensity was first normalized to the initial intensity before bleaching, then the fluorescence intensity was measured at time of prebleaching (I_0), right after photobleaching (I_1), and at 200 seconds after photobleaching (I_{200}), and recovery rate = $(I_{200} - I_1)/(I_0 - I_1)$. For melanoblasts, the number of protrusions generated from the cell body was counted manually, and the lengths of leading protrusion of melanoblasts were measured using FIJI. For quantification of melanoblasts migrating speed, the live imaging series were analyzed autonomously using the Trackmate (Tinevez et al., 2017) plugin in FIJI to generate the mean speed.

All statistical analysis was performed using GraphPad Prism 5 software and Microsoft Excel. Statistical parameters including the exact value of n, meant ± SEM or ± SD, and statistical significance were mentioned individually in their relative figure legend. Data were judged to be statistically significant when p-value < 0.05 by two-tailed paired or unpaired Student's t-test, asterisks denote statistical significance (ns = not significant, *, $p < 0.05$; **, $p < 0.01$, ***, $p < 0.001$, ****, $p < 0.0001$), as described in individual figure legend. Where no significance is indicated, p values were >0.05.

Supplementary Material

Refer to Web version on PubMed Central for supplementary material.

Acknowledgements

References

Adams JC, and Watt FM (1990). Changes in keratinocyte adhesion during terminal differentiation: reduction in fibronectin binding precedes alpha 5 beta 1 integrin loss from the cell surface. Cell 63, 425–435. [PubMed: 2145076]

Ahtiainen L, Lefebvre S, Lindfors PH, Renvoise E, Shirokova V, Vartiainen MK, Thesleff I, and Mikkola ML (2014). Directional cell migration, but not proliferation, drives hair placode morphogenesis. Dev. Cell 28, 588–602. [PubMed: 24636260]

Ali N, Zirak B, Rodriguez RS, Pauli ML, Truong H-A, Lai K, Ahn R, Corbin K, Lowe MM, and Scharschmidt TC (2017). Regulatory T cells in skin facilitate epithelial stem cell differentiation. Cell 169, 1119–1129. [PubMed: 28552347]

Amcheslavsky A, Jiang J, and Ip YT (2009). Tissue damage-induced intestinal stem cell division in Drosophila. Cell Stem Cell 4, 49–61. [PubMed: 19128792]

Andl T, Reddy ST, Gaddapara T, and Millar SE (2002). WNT signals are required for the initiation of hair follicle development. Dev. Cell 2, 643–653. [PubMed: 12015971]

Benham-Pyle BW, Pruitt BL, and Nelson WJ (2015). Cell adhesion. Mechanical strain induces E-cadherin-dependent Yap1 and beta-catenin activation to drive cell cycle entry. Science 348, 1024–1027. [PubMed: 26023140]

Cetera M, Leybova L, Joyce B, and Devenport D (2018). Counter-rotational cell flows drive morphological and cell fate asymmetries in mammalian hair follicles. Nat. Cell Biol 20, 541–552. [PubMed: 29662173]

Chen D, Jarrell A, Guo C, Lang R, and Atit R (2012). Dermal beta-catenin activity in response to epidermal Wnt ligands is required for fibroblast proliferation and hair follicle initiation. Development 139, 1522–1533. [PubMed: 22434869]

Chrostek A, Wu X, Quondamatteo F, Hu R, Sanecka A, Niemann C, Langbein L, Haase I, and Brakebusch C (2006). Rac1 is crucial for hair follicle integrity but is not essential for maintenance of the epidermis. Mol. Cell. Biol 26, 6957–6970. [PubMed: 16943436]

Discher DE, Janmey P, and Wang YL (2005). Tissue cells feel and respond to the stiffness of their substrate. Science 310, 1139–1143. [PubMed: 16293750]

Dogterom M, and Koenderink GH (2019). Actin-microtubule crosstalk in cell biology. Nat. Rev. Mol. Cell Biol 20, 38–54. [PubMed: 30323238]

Festa E, Fretz J, Berry R, Schmidt B, Rodeheffer M, Horowitz M, and Horsley V (2011). Adipocyte lineage cells contribute to the skin stem cell niche to drive hair cycling. Cell 146, 761–771. [PubMed: 21884937]

Fu J, and Hsu W (2013). Epidermal Wnt controls hair follicle induction by orchestrating dynamic signaling crosstalk between the epidermis and dermis. J. Invest. Dermatol 133, 890–898. [PubMed: 23190887]

Fuchs E, and Raghavan S (2002). Getting under the skin of epidermal morphogenesis. Nature Reviews 3, 199–209.

Fuchs E, Tumbar T, and Guasch G (2004). Socializing with the neighbors: stem cells and their niche. Cell 116, 769–778. [PubMed: 15035980]

Gasic I, Boswell SA, and Mitchison TJ (2019). Tubulin mRNA stability is sensitive to change in microtubule dynamics caused by multiple physiological and toxic cues. PLoS Biol. 17, e3000225. [PubMed: 30964857]

Goldstein J, and Horsley V (2012). Home sweet home: skin stem cell niches. Cell Mol. Life Sci 69, 2573–2582. [PubMed: 22410738]

Grose R, Hutter C, Bloch W, Thorey I, Watt FM, Fassler R, Brakebusch C, and Werner S (2002). A crucial role of beta 1 integrins for keratinocyte migration in vitro and during cutaneous wound repair. Development 129, 2303–2315. [PubMed: 11959837]

Guo Z, and Ohlstein B (2015). Bidirectional Notch signaling regulates Drosophila intestinal stem cell multipotency. Science 350.

Gur-Cohen S, Yang H, Baksh SC, Miao Y, Levorse J, Kataru RP, Liu X, de la Cruz-Racelis J, Mehrara BJ, and Fuchs E (2019). Stem cell-driven lymphatic remodeling coordinates tissue regeneration. Science 366, 1218–1225. [PubMed: 31672914]

Handorf AM, Zhou Y, Halanski MA, and Li WJ (2015). Tissue stiffness dictates development, homeostasis, and disease progression. Organogenesis 11, 1–15. [PubMed: 25915734]

Hsu YC, and Fuchs E (2012). A family business: stem cell progeny join the niche to regulate homeostasis. Nat. Rev. Mol. Cell Biol 13, 103–114. [PubMed: 22266760]

Hsu YC, Li L, and Fuchs E (2014). Emerging interactions between skin stem cells and their niches. Nat. Med 20, 847–856. [PubMed: 25100530]

Indra I, Troyanovsky RB, Shapiro L, Honig B, and Troyanovsky SM (2020). Sensing Actin Dynamics through Adherens Junctions. Cell Reports 30, 2820–2833. [PubMed: 32101754]

Ito M, Liu Y, Yang Z, Nguyen J, Liang F, Morris RJ, and Cotsarelis G (2005). Stem cells in the hair follicle bulge contribute to wound repair but not to homeostasis of the epidermis. Nat. Med 11, 1351–1354. [PubMed: 16288281]

Ito M, Yang Z, Andl T, Cui C, Kim N, Millar SE, and Cotsarelis G (2007). Wnt-dependent de novo hair follicle regeneration in adult mouse skin after wounding. Nature 447, 316–320. [PubMed: 17507982]

Jackson B, Peyrollier K, Pedersen E, Basse A, Karlsson R, Wang Z, Lefever T, Ochsenbein AM, Schmidt G, Aktories K, et al. (2011). RhoA is dispensable for skin development, but crucial for contraction and directed migration of keratinocytes. Mol. Biol. Cell 22, 593–605. [PubMed: 21209320]

Jaubert J, Patel S, Cheng J, and Segre JA (2004). Tetracycline-regulated transactivators driven by the involucrin promoter to achieve epidermal conditional gene expression. J. Invest. Dermatol 123, 313–318. [PubMed: 15245431]

Jiang H, Patel PH, Kohlmaier A, Grenley MO, McEwen DG, and Edgar BA (2009). Cytokine/Jak/Stat signaling mediates regeneration and homeostasis in the Drosophila midgut. Cell 137, 1343–1355. [PubMed: 19563763]

Jones PH, Harper S, and Watt FM (1995). Stem cell patterning and fate in human epidermis. Cell 80, 83–93. [PubMed: 7813021]

Kechagia JZ, Ivaska J, and Roca-Cusachs P (2019). Integrins as biomechanical sensors of the microenvironment. Nat. Rev. Mol. Cell Biol 20, 457–473. [PubMed: 31182865]

Klein EA, Yin L, Kothapalli D, Castagnino P, Byfield FJ, Xu T, Levental I, Hawthorne E, Janmey PA, and Assoian RK (2009). Cell-cycle control by physiological matrix elasticity and in vivo tissue stiffening. Curr. Biol 19, 1511–1518. [PubMed: 19765988]

Kovacs M, Toth J, Hetenyi C, Malnasi-Csizmadia A, and Sellers JR (2004). Mechanism of blebbistatin inhibition of myosin II. J. Biol. Chem 279, 35557–35563. [PubMed: 15205456]

Krendel M, Zenke FT, and Bokoch GM (2002). Nucleotide exchange factor GEF-H1 mediates cross-talk between microtubules and the actin cytoskeleton. Nat. Cell Biol 4, 294–301. [PubMed: 11912491]

le Duc Q, Shi Q, Blonk I, Sonnenberg A, Wang N, Leckband D, and de Rooij J (2010). Vinculin potentiates E-cadherin mechanosensing and is recruited to actin-anchored sites within adherens junctions in a myosin II-dependent manner. The Journal of Cell Biology 189, 1107–1115. [PubMed: 20584916]

Le HQ, Ghatak S, Yeung CY, Tellkamp F, Gunschmann C, Dieterich C, Yeroslaviz A, Habermann B, Pombo A, Niessen CM, et al. (2016). Mechanical regulation of transcription controls Polycomb-mediated gene silencing during lineage commitment. Nat. Cell Biol 18, 864–875. [PubMed: 27398909]

Liang J, Balachandra S, Ngo S, and O'Brien LE (2017). Feedback regulation of steady-state epithelial turnover and organ size. Nature 548, 588–591. [PubMed: 28847000]

Mondal BC, Mukherjee T, Mandal L, Evans CJ, Sinenko SA, Martinez-Agosto JA, and Banerjee U (2011). Interaction between differentiating cell- and niche-derived signals in hematopoietic progenitor maintenance. Cell 147, 1589–1600. [PubMed: 22196733]

Mort RL, Jackson IJ, and Patton EE (2015). The melanocyte lineage in development and disease. Development 142, 620–632. [PubMed: 25670789]

Muroyama A, and Lechler T (2017). A transgenic toolkit for visualizing and perturbing microtubules reveals unexpected functions in the epidermis. eLife 6, e29834. [PubMed: 28869035]

Muroyama A, Terwilliger M, Dong B, Suh H, and Lechler T (2018). Genetically induced microtubule disruption in the mouse intestine impairs intracellular organization and transport. Mol. Biol. Cell 29, 1533–1541. [PubMed: 29742015]

Nagae S, Meng W, and Takeichi M (2013). Non-centrosomal microtubules regulate F-actin organization through the suppression of GEF-H1 activity. Genes Cells 18, 387–396. [PubMed: 23432781]

Ouspenskaia T, Matos I, Mertz AF, Fiore VF, and Fuchs E (2016). WNT-SHH Antagonism Specifies and Expands Stem Cells prior to Niche Formation. Cell 164, 156–169. [PubMed: 26771489]

Pellegrin S, and Mellor H (2007). Actin stress fibres. J. Cell Sci 120, 3491–3499. [PubMed: 17928305]

Raghavan S, Bauer C, Mundschau G, Li Q, and Fuchs E (2000). Conditional ablation of beta1 integrin in skin. Severe defects in epidermal proliferation, basement membrane formation, and hair follicle invagination. The Journal of Cell Biology 150, 1149–1160. [PubMed: 10974002]

Rao MV, and Zaidel-Bar R (2016). Formin-mediated actin polymerization at cell-cell junctions stabilizes E-cadherin and maintains monolayer integrity during wound repair. Mol. Biol. Cell 27, 2844–2856. [PubMed: 27440924]

Rodriguez OC, Schaefer AW, Mandato CA, Forscher P, Bement WM, and Waterman-Storer CM (2003). Conserved microtubule-actin interactions in cell movement and morphogenesis. Nat. Cell Biol 5, 599–609. [PubMed: 12833063]

Samuel MS, Lopez JI, McGhee EJ, Croft DR, Strachan D, Timpson P, Munro J, Schroder E, Zhou J, Brunton VG, et al. (2011). Actomyosin-mediated cellular tension drives increased tissue stiffness and beta-catenin activation to induce epidermal hyperplasia and tumor growth. Cancer Cell 19, 776–791. [PubMed: 21665151]

Sharp LL, Jameson JM, Cauvi G, and Havran WL (2005). Dendritic epidermal T cells regulate skin homeostasis through local production of insulin-like growth factor 1. Nat. Immunol 6, 73–79. [PubMed: 15592472]

Snippert HJ, van der Flier LG, Sato T, van Es JH, van den Born M, Kroon-Veenboer C, Barker N, Klein AM, van Rheenen J, Simons BD, et al. (2010). Intestinal crypt homeostasis results from neutral competition between symmetrically dividing Lgr5 stem cells. Cell 143, 134–144. [PubMed: 20887898]

Subramanian A, Tamayo P, Mootha VK, Mukherjee S, Ebert BL, Gillette MA, Paulovich A, Pomeroy SL, Golub TR, Lander ES, et al. (2005b). Gene set enrichment analysis: a knowledge-based approach for interpreting genome-wide expression profiles. Proc. Natl. Acad. Sci. USA 102, 15545–15550. [PubMed: 16199517]

Sumigray KD, Foote HP, and Lechler T (2012). Noncentrosomal microtubules and type II myosins potentiate epidermal cell adhesion and barrier formation. J. Cell. Biol 199, 513–525. [PubMed: 23091070]

Tadokoro T, Gao X, Hong CC, Hotten D, and Hogan BL (2016). BMP signaling and cellular dynamics during regeneration of airway epithelium from basal progenitors. Development 143, 764–773. [PubMed: 26811382]

Tata PR, and Rajagopal J (2016). Regulatory Circuits and Bi-directional Signaling between Stem Cells and Their Progeny. Cell Stem Cell 19, 686–689. [PubMed: 27912089]

Tinevez JY, Perry N, Schindelin J, Hoopes GM, Reynolds GD, Laplantine E, Bednarek SY, Shorte SL, and Eliceiri KW (2017). TrackMate: An open and extensible platform for single-particle tracking. Methods 115, 80–90. [PubMed: 27713081]

Tomann P, Paus R, Millar SE, Scheidereit C, and Schmidt-Ullrich R (2016). Lhx2 is a direct NF-kappaB target gene that promotes primary hair follicle placode down-growth. Development 143, 1512–1522. [PubMed: 26952977]

Tsai SY, Sennett R, Rezza A, Clavel C, Grisanti L, Zemla R, Najam S, and Rendl M (2014). Wnt/beta-catenin signaling in dermal condensates is required for hair follicle formation. Dev. Biol 385, 179–188. [PubMed: 24309208]

Valon L, Marin-Llaurado A, Wyatt T, Charras G, and Trepat X (2017). Optogenetic control of cellular forces and mechanotransduction. Nat. Commun 8, 14396. [PubMed: 28186127]

Verma S, Han SP, Michael M, Gomez GA, Yang Z, Teasdale RD, Ratheesh A, Kovacs EM, Ali RG, and Yap AS (2012). A WAVE2-Arp2/3 actin nucleator apparatus supports junctional tension at the epithelial zonula adherens. Mol. Biol. Cell 23, 4601–4610. [PubMed: 23051739]

Vicente-Manzanares M, Ma X, Adelstein RS, and Horwitz AR (2009). Non-muscle myosin II takes centre stage in cell adhesion and migration. Nat. Rev. Mol. Cell Biol 10, 778–790. [PubMed: 19851336]

Wang J, Vasaikar S, Shi Z, Greer M, and Zhang B (2017). WebGestalt 2017: a more comprehensive, powerful, flexible and interactive gene set enrichment analysis toolkit. Nucleic Acids Res. 45, W130–W137. [PubMed: 28472511]

Wang Y, Wang G, Luo X, Qiu J, and Tang C (2012). Substrate stiffness regulates the proliferation, migration, and differentiation of epidermal cells. Burns 38, 414–420. [PubMed: 22037151]

Watt FM (2002). Role of integrins in regulating epidermal adhesion, growth and differentiation. EMBO J. 21, 3919–3926. [PubMed: 12145193]

Watt FM, and Fujiwara H (2011). Cell-extracellular matrix interactions in normal and diseased skin. Cold Spring Harb. Perspect. Biol 3, a005124. [PubMed: 21441589]

Watt FM, and Huck WT (2013). Role of the extracellular matrix in regulating stem cell fate. Nat. Rev. Mol. Cell Biol 14, 467–473. [PubMed: 23839578]

Yonemura S, Wada Y, Watanabe T, Nagafuchi A, and Shibata M (2010). alpha-Catenin as a tension transducer that induces adherens junction development. Nat. Cell Biol 12, 533–542. [PubMed: 20453849]

Zaidel-Bar R, Zhenhuan G, and Luxenburg C (2015). The contractome--a systems view of actomyosin contractility in non-muscle cells. Journal of Cell Science 128, 2209–2217. [PubMed: 26021351]

Zhang H, Pasolli HA, and Fuchs E (2011). Yes-associated protein (YAP) transcriptional coactivator functions in balancing growth and differentiation in skin. Proc. Natl. Acad. Sci. USA 108, 2270–2275. [PubMed: 21262812]

Zhang Y, Tomann P, Andl T, Gallant NM, Huelsken J, Jerchow B, Birchmeier W, Paus R, Piccolo S, Mikkola ML, et al. (2009). Reciprocal requirements for EDA/EDAR/NF-kappaB and Wnt/beta-catenin signaling pathways in hair follicle induction. Dev. Cell 17, 49–61. [PubMed: 19619491]
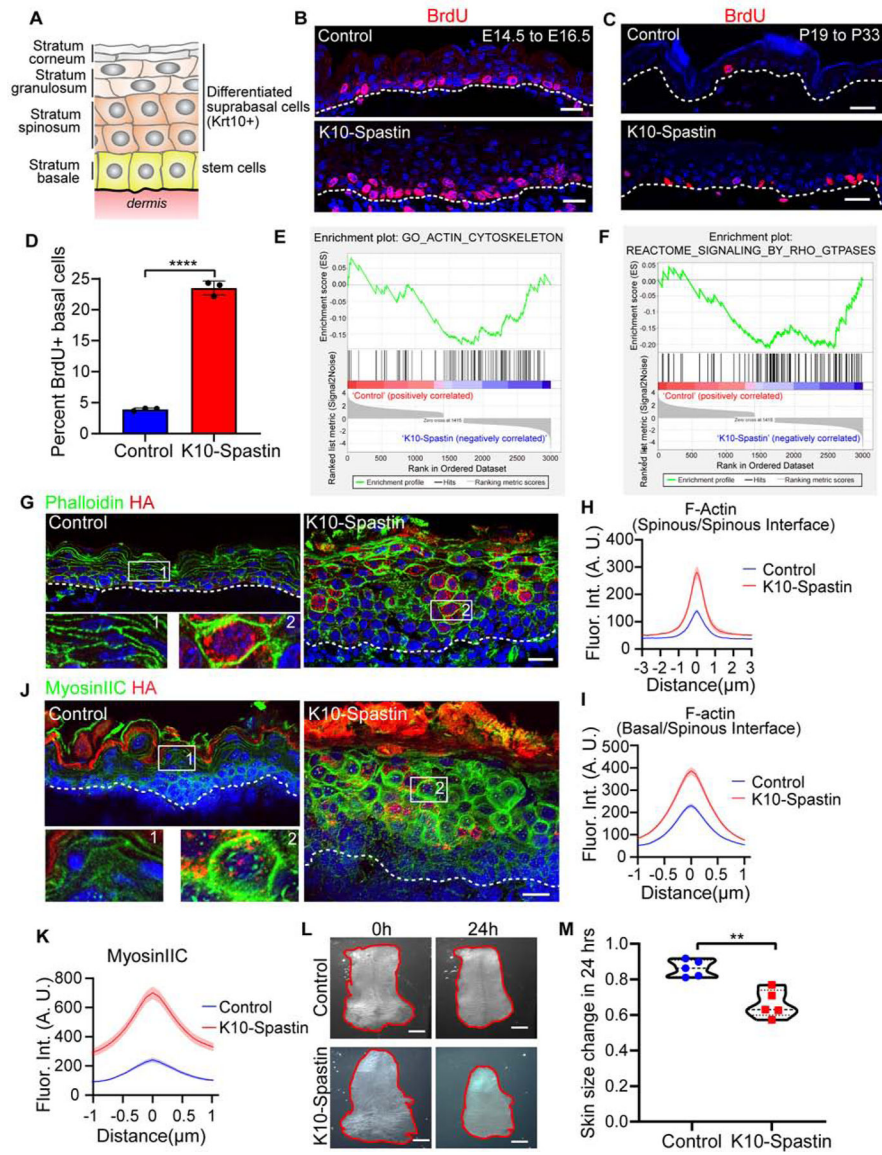
Figure 1. Microtubule disruption increases cortical actomyosin

(A) Schematic of the stratified epidermis with basal stem cells and their progeny-Krt10+ differentiated suprabasal cells.

(B and C) BrdU (red) immunofluorescence staining in control and K10-Spastin epidermis at E16.5 (B), and in adult (C). Embryos/mice were exposed to doxycycline from E14.5–16.5 for (B) and from P19–33 for (C). Scale bars, 20 μm.

(D) Percentage of BrdU+ basal cells in treated adult backskin epidermis. Data is mean ± SD, n=3 mice for control (36 fields) and K10-Spastin (38 fields), p-value<0.0001, two-tailed unpaired t-test.

(E and F) Gene Set Enrichment Analysis (GSEA) of RNA-Seq data for control and K10-Spastin, revealing an actin cytoskeleton gene signature (E) and Rho-GTPase reactome signaling related genes (F) enriched in K10-Spastin. Normalized enrichment score (NES):

−1.42, FDR: 0.016, p-value: 0.003 for (E); and NES: −1.56, FDR: 0.0125, p-value: 0.003 for (F).

(G) Immunofluorescence staining of F-actin labeled by phalloidin (green) and HA-Spastin (red) in the epidermis at E16.5. Embryos were exposed to doxycycline from E14.5. Scale bar, 20 μm.

(H) Quantification of F-actin fluorescence intensity at spinous cell-spinous cell boundaries in control and K10-Spastin. Data is mean ± SEM, n=38 cells for control and n=39 cells for K10-Spastin from 3 embryos, p-value <0.0001, two-tailed unpaired t-test.

(I) Quantification of interface F-actin intensity between spinous and basal cells. In the K10-Spastin epidermis, only the interface F-actin between HA+ spinous and basal cells was measured. Data is mean ± SEM, n=61 cells for control and n=86 cells for K10-Spastin from 3 embryos, p-value <0.0001, two-tailed unpaired t-test.

(J) Immunofluorescence staining of cortical MyosinIIC (green) and Spastin-HA (red) at E16.5, doxycycline was added at E14.5. Scale bar, 20 μm.

(K) Quantification of MyosinIIC fluorescence intensity at cell-cell boundaries of suprabasal cells. Data is mean ± SEM, n=40 cells for control and n=50 cells for K10-Spastin from 3 embryos, p-value <0.0001, two-tailed unpaired t-test.

(L) Skin explants of control and K10-Spastin at the beginning (E15.5) and 24 hours later (sustained with 2 μg/ml doxycycline). Scale bars, 1mm.

(M) Changes of skin explant area over 24 hours. Shown are violin plots with each measurement being the skin from a distinct embryo, n=5 embryos for control and K10-Spastin from 3 litters were measured, p-value<0.01, two-tailed unpaired t-test.
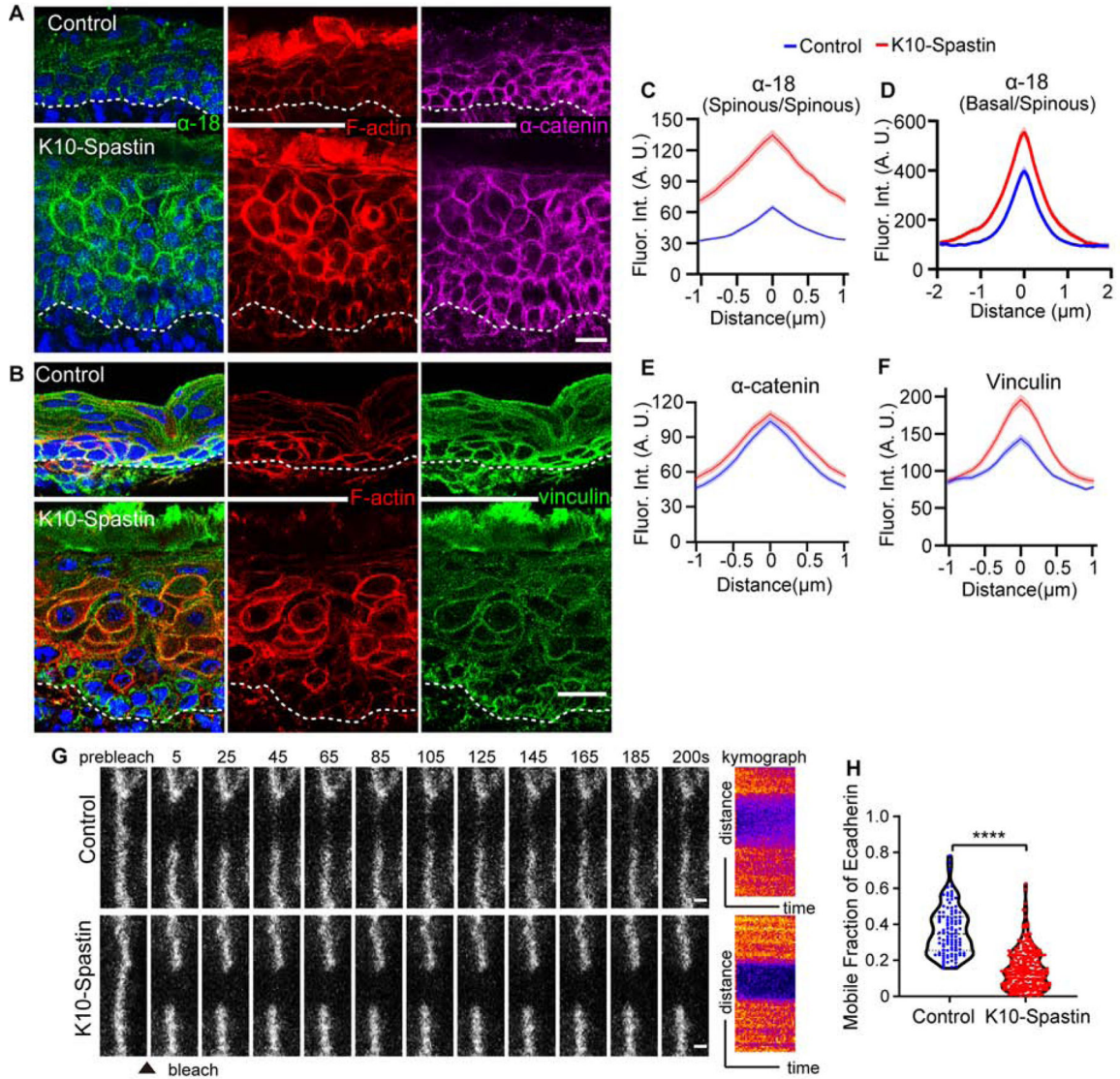
Figure 2. Microtubule depolymerization increases adherens junctional tension and stability

(A) Immunofluorescence staining of α−18 (green), F-actin (red) and α-catenin (magenta) in control and K10-Spastin epidermis. Scale bar, 20 μm.

(B) Co-staining of vinculin (green) and F-actin (red) in control and K10-Spastin epidermis. Scale bar, 20 μm.

(C) Quantification of α−18 fluorescence intensity at cell-cell boundaries of spinous cells. Data is mean ± SEM, n=35 cells for control and n=42 cells for K10-Spastin from 3 embryos, p-value <0.0001, two-tailed unpaired t-test.

(D) Quantification of α−18 intensity between spinous and basal cells. In K10-Spastin, only α−18 at the interface between HA+ spinous and basal cells was measured. Data is mean ± SEM, n=44 cells for control and n=49 cells for K10-Spastin from 3 embryos, p-value <0.0001, two-tailed unpaired t-test.

(E) Quantification of α-catenin fluorescence intensity at cell-cell boundaries of suprabasal cells in control and K10-Spastin epidermis. Data is mean ± SEM, n=40 cells for control and n=41 cells for K10-Spastin from 3 embryos, p-value = 0.205, two-tailed unpaired t-test.

(F) Quantification of vinculin fluorescence intensity at cell-cell boundaries of suprabasal cells in control and K10-Spastin epidermis. Data is mean ± SEM, n=29 cells for control and K10-Spastin from 2 embryos, p-value <0.0001, two-tailed unpaired t-test.

(G) Time-lapse series of E-cadherin-CFP FRAP in suprabasal cells in control and K10-Spastin epidermis at E15.5. Kymograph of E-cadherin-CFP over 200 seconds is shown on the right. Scale bars, 1 μm.

(H) Quantification of E-cadherin-CFP recovery rate after 200 seconds following photobleaching in suprabasal cells. For control, n=107 regions from 6 embryos, for K10-Spastin, n= 305 regions from 3 embryos, p-value<0.0001, two-tailed unpaired t-test.
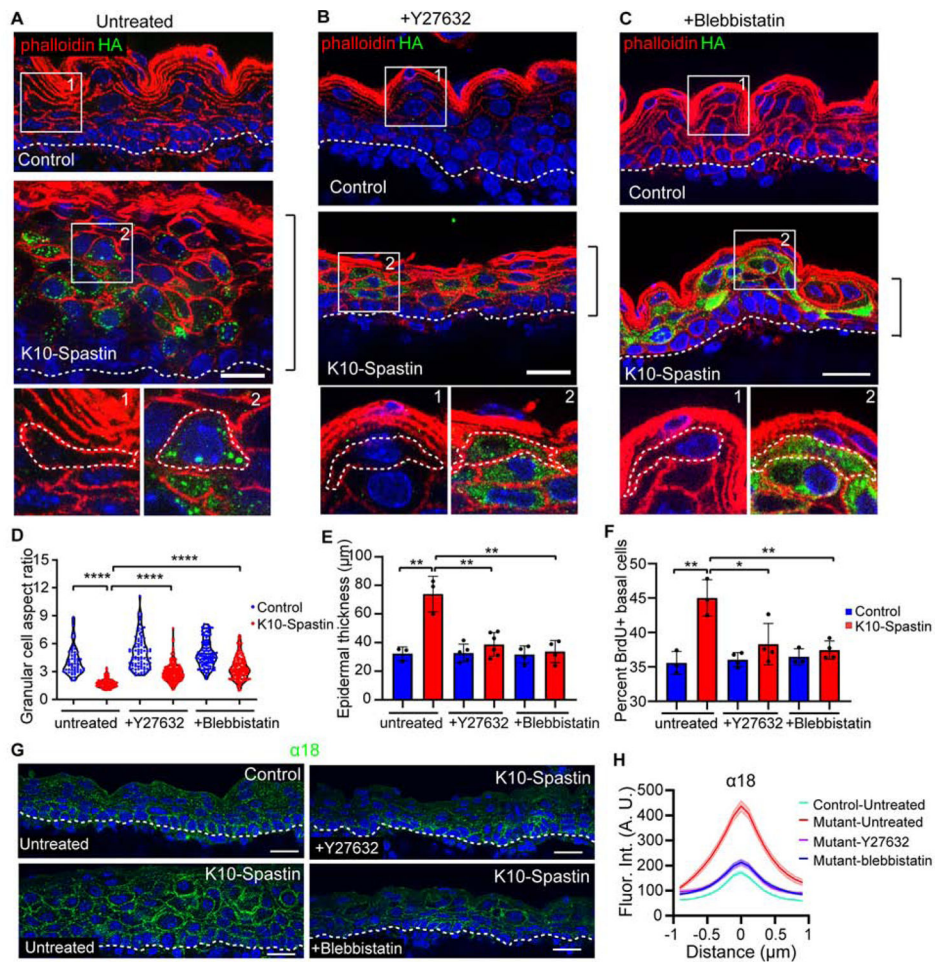
Figure 3. Decreasing contractility rescues skin thickness, cell shape and basal cell hyperproliferation caused by microtubule disruption in suprabasal cells

(A-C) Immunofluorescence staining of Spastin-HA (green) and F-actin (red) in untreated (A), Y27632 (B), and blebbistatin (C) injected control and K10-Spastin epidermis, respectively. Scale bars, 20 μm.

(D) Quantification of granular cell aspect ratio in untreated, Y27632, and blebbistatin treated control and K10-Spastin epidermis. Each point represents a single cell. For the untreated condition, n=58 cells for control and n=102 cells for K10-Spatin from 3 embryos. For Y27632, n=83 cells for control and n=171 cells for K10-Spastin from 4 embryos. For blebbistatin, n=105 cells for control and n=146 cells for K10-Spastin from 4 embryos. p-value<0.0001, two-tailed unpaired t-test.

(E) Quantification of skin thickness in untreated, Y27632, and blebbistatin treated control and K10-Spastin epidermis. Data is mean ± SD. For untreated condition, n=3 embryos for control (89 regions) and K10-Spastin (102 regions) from 2 untreated litters were measured. For Y27632, n=5 embryos for control (182 regions) and n=6 embryos for K10-Spastin (255 regions) from 3 injected litters were measured. For blebbistatin, n=4 embryos for control (133 regions) and K10-Spastin (214 regions) from 3 injected litters were measured. p-value<0.01, two-tailed unpaired t-test.

(F) Percentage of BrdU+ basal cells in untreated, Y27632, and Blebbistatin treated control and K10-Spastin epidermis. Data is mean ± SD. For untreated, n=3 embryos for control (31 fields) and K10-Spastin (40 fields). For Y27632, n=4 embryos for control (32 fields) and K10-Spastin (38 fields). For blebbistatin, n=3 embryos for control (31 fields) and n=4 embryos for K10-Spastin (47 fields). For the analysis: control to K10-Spastin untreated group: p-value<0.01; K10-Spastin untreated to Y27632 treated group: p-value=0.0279; K10-Spastin untreated to blebbistatin treated group: p-value<0.01; all are two-tailed unpaired t-test.

(G) Staining of α−18 in untreated control, untreated and drug treated K10-Spastin epidermis at E16.5. Scale bars, 20 μm.

(H) Measurement of cortical α−18 in untreated control, untreated and drug treated K10-Spastin epidermis. Data is mean ± SEM, n=36 cells for untreated control, n=44 cells for untreated K10-Spatin, n=42 cells for Y-27632 treated K10-Spastin, and n=45 cells for blebbistatin treated K10-Spastin, 3 embryos for all conditions were measured. For untreated to Y-27632 or blebbistatin K10-Spastin, and untreated K10-Spastin to control, p-value<0.0001, two-tailed unpaired t-test.
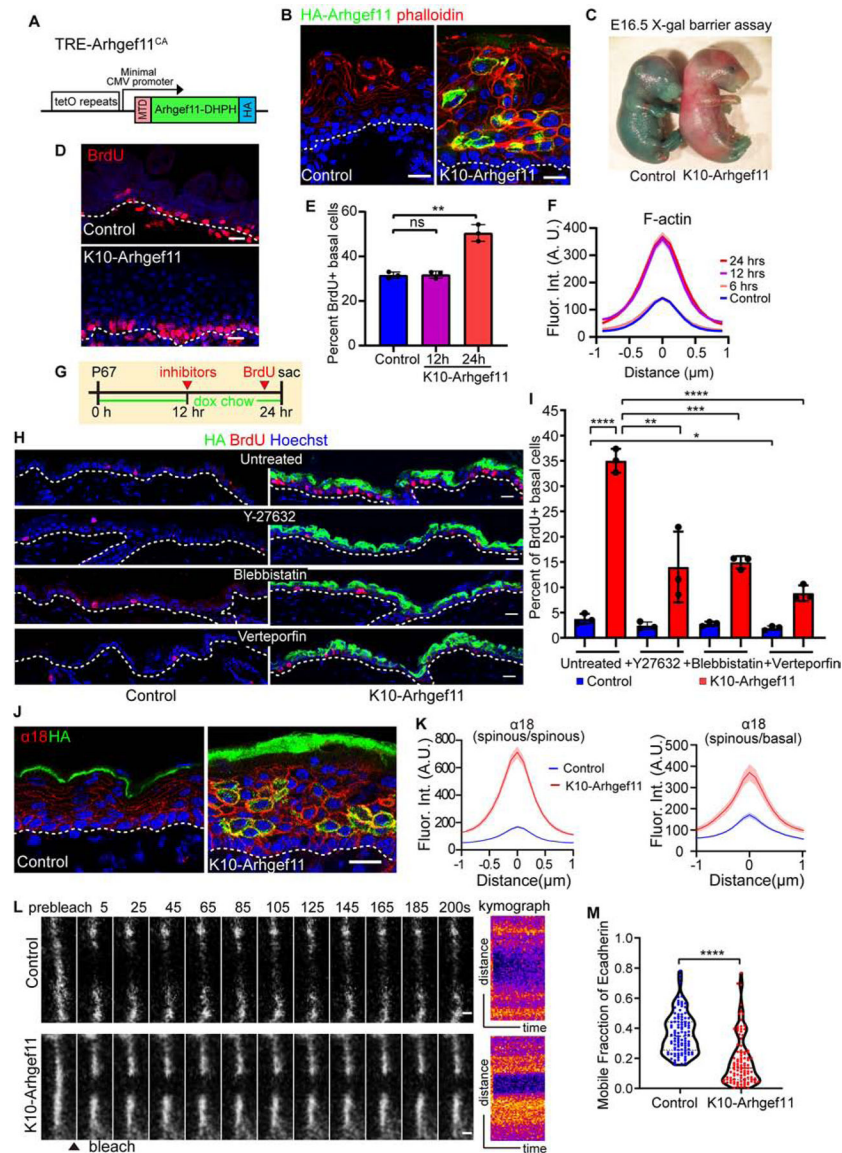
Figure 4. RHO-GEF induced contractility stabilizes adherens junction and induces stem cell proliferation

(A) Diagram of the TRE-Arhgef11^{CA} transgene. Arhgef11-DHPH was tagged with a membrane targeting domain (MTD) at the N-terminus and an HA tag at the C-terminus.

(B) Co-staining of F-actin (phalloidin, red) and Arhgef11-HA (green) in the epidermis of control and K10-Arhgef11 at E17.5, doxycycline since E13.5. Scale bars, 20 μm.

(C) Skin X-gal barrier assay of E16.5 control and K10-Arhgef11 embryos. Absence of dye indicates an effective outside-in barrier.

(D) BrdU staining in control and K10-Arhgef11 epidermis at E17.5, doxycycline-treated from E13.5. Scale bar, 20 μm.

(E) Percentage of BrdU+ basal cells in control and K10-Arhgef11 E16.5 embryos, 12 and 24 hrs after doxycycline administration. Data is mean ± SD, n=3 embryos for control (16 fields) and K10-Arghef11 – 12 hrs (14 fields) and 24 hrs (17 fields) of K10-Arhgef11. For control to 12 hrs, p-value=0.8488, for control to 24 hrs, p-value<0.01, two-tailed unpaired t-test.

(F) Fluorescence intensity of cortical F-actin in control and K10-Arghef11 E16.5 embryos, 6, 12 and 24 hrs after doxycycline administration. Data is mean ± SEM, n=35 cells for control (3 embryos); n=37 cells for 6 hrs (2 embryos), n=42 cells for 12 hrs (3 embryos), and n=35 cells for 24 hrs (3 embryos) of K10-Arhgef11. For 6 hrs to control, p-value=0.876; 12 hrs to control, p-value<0.0001; for 12 hrs to 24 hrs, p-value=0.719, two-tailed unpaired t-test.

(G) Diagram depicting the drug injection time in K10-Arhgef11. Mice at P67 were fed with doxycycline chow, injected with inhibitors after 12 hours on doxycycline, and injected with BrdU 1 hour before sacrifice at 24 hr.

(H) Immunofluorescence staining of BrdU in untreated, Y27632, blebbistatin and verteporfin treated control (left) and K10-Arhgef11 (right) adult epidermis. Scale bars, 20 μm.

(I) Percentage of BrdU+ basal cells in untreated, Y27632, blebbistatin and verteporfin treated control and K10-Arhgef11 adult epidermis. Data is mean ± SD, n=3 mice for all groups, for untreated control (30 fields) and K10-Arhgef11 (33 fields), for Y-27632 treated control (22 fields) and K10-Arhgef11 (38 fields), for blebbistatin treated control (32 fields) and K10-Arhgef11 (35 fields), and for verteporfin treated control (31 fields) and K10-Arhgef11 (36 fields) were measured. For the analysis: untreated control to K10-Arhgef11, p-value<0.0001; untreated to Y-27632 treated control, p=0.1336; untreated to blebbistatin treated control, p=0.1991; untreated to verteporfin treated control, p<0.05; untreated to Y-27632 treated K10-Arhgef11, p<0.01; untreated to blebbistatin treated K10-Arhgef11, p<0.001; untreated to verteporfin treated K10-Arhgef11, p<0.0001; all are two-tailed unpaired t-test.

(J) Co-staining of α−18 (red) and Arhgef11-HA (green) in control and K10-Arhgef11 epidermis at E17.5. Scale bar, 20 μm.

(K) Left: Quantification of cortical α−18 fluorescence intensity in control and K10-Arhgef11 spinous cells. Data is mean ± SEM, n=35 cells for control and n=51 cells for K10-Arhgef11 from 3 embryos, p-value <0.0001, two-tailed unpaired t-test. Right: Quantification of α−18 intensity at the interface between basal and spinous cells. In K10-Arhgef11, only α−18 at the interface between HA+ spinous and basal cells was measured. Data is mean ± SEM, n=26 cells for control and n=23 cells for K10-Arhgef11 from 3 embryos, p-value <0.0001, two-tailed unpaired t-test.

(L) Time-lapse series of E-cadherin-CFP FRAP in suprabasal cells in control and K10-Arhgef11 epidermis at E15.5. Kymograph of E-cadherin-CFP over 200 seconds is shown on the right. Scale bars, 1 μm.

(M) Quantification of E-cadherin-CFP recovery rate in 200 seconds after photobleaching in suprabasal cells. Note that the dataset displayed for the control here is the same as in Figure 2H. For control, n=107 regions from 6 embryos, for K10-Arhgef11, n= 102 regions from 3 embryos, p-value<0.0001, two-tailed unpaired t-test.
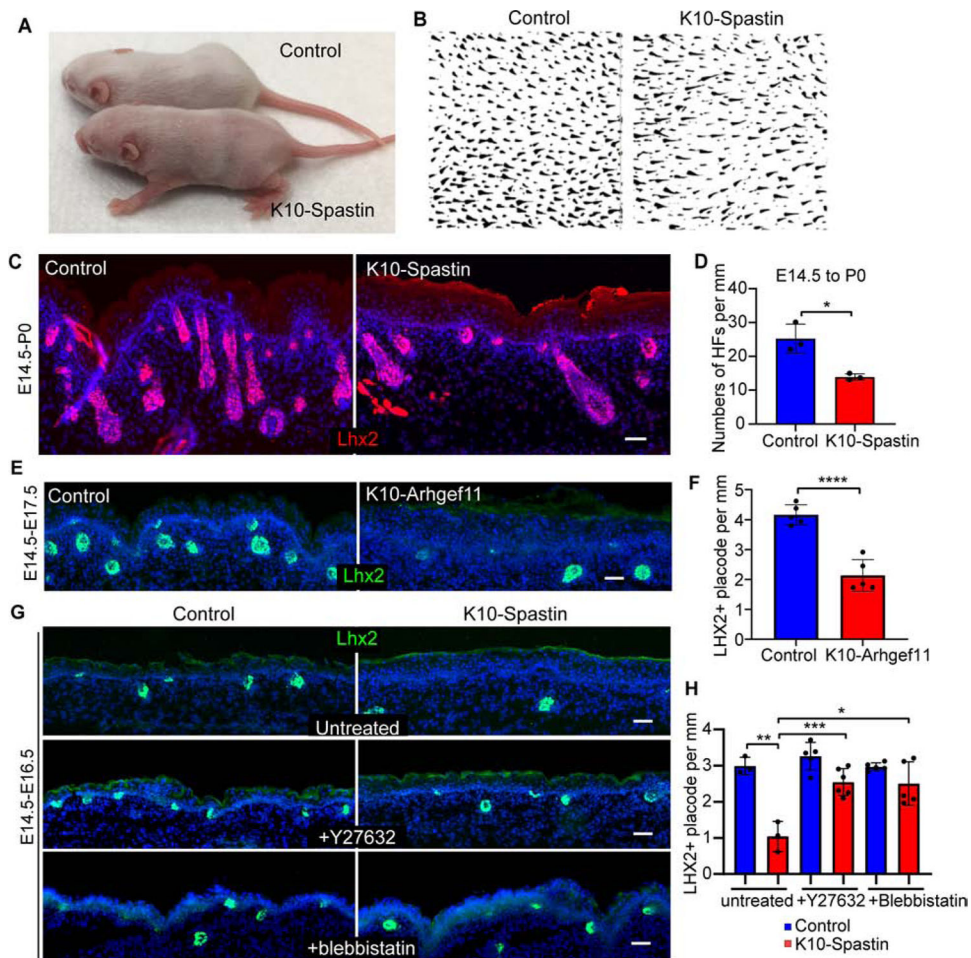
Figure 5. Increased contractility in differentiated cells causes non-cell autonomous defects in hair follicles formation

(A) Decreased hair coat in K10-Spastin mice at P8. Spastin expression was induced at E16.5 with doxycycline.

(B) Whole mount of hair follicles in K10-Spastin and control mice.

(C and D) Staining of LHX2 (red) to mark hair follicles in control and K10-spastin epidermis at P0. Expression was induced at E14.5. Scale bar, 50 μm. Data is mean ± SD, n=3 embryos for control (24 fields) and K10-Spastin (31 fields), p-value= 0.0108, two-tailed unpaired t-test.

(E and F) Staining of LHX2 (green) in control and K10-Arhgef11 epidermis at E17.5. Expression was induced at E14.5. Scale bar, 50 μm. Data is mean ± SD, n=5 embryos for control (62 fields) and K10-Arhgef11 (52 fields), p-value <0.0001, two-tailed unpaired t-test.

(G and H) Staining of LHX2 (green) in untreated, Y27632 or blebbistatin treated control and K10-Spastin embryos at E16.5. Expression was induced at E14.5. Scale bars, 50 μm. Data is mean ± SD. For untreated, n=3 embryos for control (36 fields) and K10-Spastin (46 fields). For Y27632, n=5 embryos for control (60 fields) and n=6 embryos for K10-Spastin (68 fields). For blebbistatin, n=5 embryos for control (65 fields) and K10-Spastin (70 fields). For the analysis: control to K10-Spastin untreated: p-value<0.01; K10-Spastin untreated to

Y27632 treated: p-value<0.001; K10-Spastin untreated to blebbistatin treated: p-value= 0.0107; two-tailed unpaired t-test.
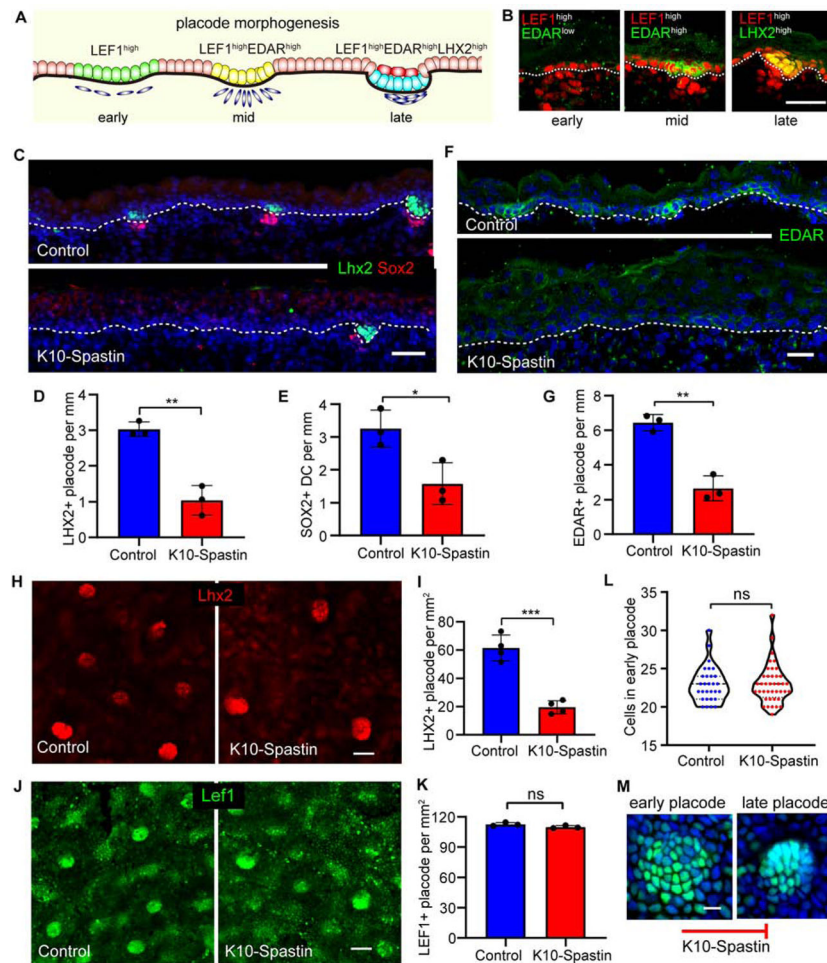
Figure 6. Increasing contractility in differentiated cells inhibits placode progression but not specification

(A) Diagram depicting stages of hair placode morphogenesis with LEF1 (green)/EDAR (yellow)/LHX2 (cyan). Sox9 cells (red) are a suprabasal cell population that forms during placode morphogenesis.

(B) Immunostaining of Lef1^{high} (red) early placode, EDAR^{high} mid placode, Lhx2^{high} late placode at E16.5. Scale bar, 30 μm.

(C) Co-staining of Lhx2 (green) and Sox2 (red) in control and K10-Spastin skin at E16.5. Expression induced at E14.5. Scale bar, 50 μm.

(D) Quantitation of Lhx2+ placodes in control and K10-Spastin E16.5 embryos. The data source is the same as in Figure 5H. Data is mean ± SD. n=3 embryos for control (36 fields) and K10-Spastin (46 fields), p-value<0.01, two-tailed unpaired t-test.

(E) Quantification of Sox2+ dermal condensates (DC) in control and K10-Spastin embryos. Data is mean ± SD, n=3 embryos for control (36 fields) and K10-Spastin (41 fields), p-value=0.0266, two-tailed unpaired t-test.

(F and G) Decreased numbers of EDAR+ placodes in K10-Spastin compared to control at E16.5. Expression was induced at E14.5. Scale bar, 20 μm. Data is mean ± SD, n=3 embryos for control (51 fields) and for K10-Spastin (61 fields), p-value<0.01, two-tailed unpaired t-test.

(H and I) Decreased Lhx2+ placodes in K10-Spastin compared to control by whole mount staining of the epidermis at E16.5. Expression induced at E14.5. Scale bar, 40 μm. Data is mean ± SD, n=4 embryos for control (27 fields) and for K10-Spastin (28 fields), p-value<0.001, two-tailed unpaired t-test.

(J and K) Quantification of LEF1+ placodes (including early and late placode stages) in control and K10-Spastin embryos at E16.5. Expression was induced at E14.5. Scale bar, 40 μm. Data is mean ± SD, n=3 embryos for control (13 fields) and K10-Spastin (19 fields), p-value=0.1054 (>0.05, not significant), two-tailed unpaired t-test.

(L) Quantification of LEF1+ cell numbers in early placodes of control and K10-Spastin embryos at E16.5. n=29 placodes for control and n=40 placodes for K10-Spastin from 3 embryos, p-value=0.9546 (>0.05, not significant), two-tailed unpaired t-test.

(M) Images of LEF1-labeled early and late placode, the progression of which is blocked in K10-Spastin embryos. Scale bar, 10 μm.
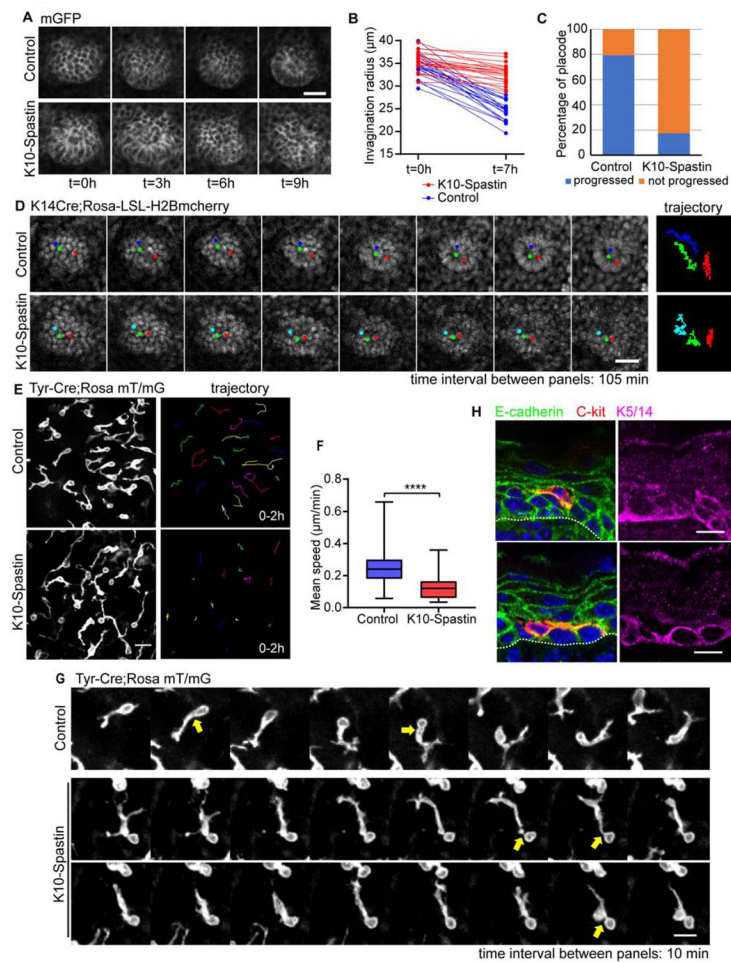
Figure 7. Increased contractility of differentiated epidermal cells decreases cell migration of placodal cells and melanoblasts

(A) Time-lapse series of placode progression in control and K10-Spastin epidermis at E15.5, cell membranes are marked with a membrane-GFP. Scale bar, 20 μm.

(B) Quantification of placode radius in control and K10-Spastin skin, showing changes in placode size after 7 hours of imaging. n=20 placodes for control and n=22 placodes for K10-Spastin from 3 embryos. For radius ratios [(0h-7h)/0h] between control and K10-Spastin, p-value<0.0001, two-tailed unpaired t-test.

(C) Percentage of placodes that progress in control and K10-Spastin embryos, n=58 placodes for control and n=46 placodes for K10-Spastin from 3 embryos.

(D) Time-lapse series and trajectories of H2B-mCherry labeled placode progress in control and K10-Spastin epidermis imaged at E15.5. Each time interval is 105 minutes. Scale bar, 20 μm.

(E) Image of melanoblasts, as labeled by Tyr-Cre;Rosa mT/mG, in control and K10-Spastin skin at E15.5. The image on the right traces the movement of cells over a 2 hour imaging period. Scale bar, 20 μm.

(F) Quantification of the mean speed of melanoblasts in control and K10-Spastin epidermis. Data is mean ± SD, n=484 melanoblasts from 4 embryos of control, and n=572 melanoblasts

from 3 embryos of K10-Spastin were measured using the Trackmate plugin in FIJI, p-value<0.0001, two-tailed unpaired t-test.

(G) Time-lapse series of individual melanoblasts migrating in control and K10-Spastin epidermis, imaged at E15.5. Arrows indicate the broader and larger protrusion next to the cell body in control melanoblasts. Scale bar: 10 μm, time interval: 10 minutes.

(H) Co-staining of E-cadherin (green), the melanoblast marker C-kit (red) and the basal cell marker (K5/14) in control epidermis at 16.5. Scale bars, 10 μm.

KEY RESOURCES TABLE

REAGENT or RESOURCE	SOURCE	IDENTIFIER
Antibodies		
Rabbit anti-HA	Abcam	Cat#: ab9110, RRID:AB_307019
Rat anti-HA	Roche	Cat#: 11867423001, RRID:AB_390918
Chicken anti-keratin 5/14	Generated in the Lechler Lab	N/A
Rabbit anti-keratin 10	BioLegend	Cat#: 905401, RRID:AB_2565049
Rat anti-BrdU	Abcam	Cat#: ab6326, RRID:AB_305426
Rat anti-β4 integrin	BD Biosciences	Cat#: 553745, RRID:AB_395027
Rabbit anti Myosin IIA	Biolegend	Cat#: 909801, RRID:AB_2565100
Rabbit anti Myosin IIB	Biolegend	Cat#: 909901, RRID:AB_2565101
Rabbit anti Myosin IIC	Biolegend	Cat#: 919201, RRID:AB_2565209
Rabbit anti α-catenin	Sigma-Aldrich	Cat#: C2081, RRID:AB_476830
Rat anti-α−18	gift from Akira Nagafuchi	(Yonemura et al., 2010)
Mouse anti Vinculin	Sigma-Aldrich	Cat#: V9131, RRID:AB_477629
Rabbit anti-YAP/TAZ	Cell Signaling Technology	Cat#: 8418, RRID:AB_10950494
Goat anti-LHX2	Santa Cruz Biotechnology	Cat#: sc-19344, RRID:AB_2135660
Rabbit anti-SOX9	Millipore	Cat#: AB5535, RRID:AB_2239761
Goat anti-EDAR	EDAR	Cat#: AF745, RRID:AB_355565
Rabbit anti-LEF1	Cell Signaling Technology	Cat#: 2230, RRID:AB_823558
Mouse anti-E-cadherin	BD Biosciences	Cat#: 610182, RRID:AB_397581
Rabbit anti-c-Kit	Cell Signaling Technology	Cat#: 3074, RRID:AB_1147633
Mouse anti-Desmoglein 1	BD Biosciences	Cat#: 610273, RRID:AB_2093422
Mouse anti-Desmoplakin	Millipore	Cat# CBL173, RRID:AB_93346
Phalloidin-TRITC	Sigma-Aldrich	Cat#: P1951, RRID:AB_2315148
Alexa Fluor 488 Phalloidin	Invitrogen	A12379
Rabbit anti-GAPDH	Abcam	Cat#: ab9485, RRID:AB_307275
IRDye 680RD Donkey anti-Rabbit IgG	LI-COR Biosciences	Cat#: 926–68073, RRID:AB_10954442
IRDye 800CW Goat anti-Rabbit IgG	LI-COR Biosciences	Cat#: 925–32211, RRID:AB_2651127
Chemicals, Peptides, and Recombinant Proteins		
BrdU	Sigma-Aldrich	Cat#:B5002-100MG
Y-27632 2HCl	Selleckchem	Cat#: S1049
Blebbistatin	Sigma-Aldrich	Cat#: B0560
Verteporfin	VWR/US pharm conv	Cat#: 1711461
Doxycycline	Sigma-Aldrich	Cat#:D9891–1G
Fetal Bovine Serum	Mediatech	Cat#: 35–010-CV
Penicillin/Streptomycin	Gibco	Cat#:10378016
DMEM	Gibco	Cat#: No. 11965
Dispase II	Roche	Cat#: 4942078001

REAGENT or RESOURCE	SOURCE	IDENTIFIER
Trypsin-EDTA (0.25%)	Gibco	Cat#: 25200056
Versene Solution	Gibco	Cat#: 15040066
Deoxyribonuclease I	Sigma-Aldrich	Cat#:D5025–15KU
Propidium iodide solution	Sigma-Aldrich	Cat#: P4864
Albumin bovine serum	Sigma-Aldrich	Cat#:A7906–100g
Donkey serum	Sigma-Aldrich	Cat#: D9663
Goat Serum	Gibco	Cat#: 16210–064
Critical Commercial Assays		
RNAeasy Mini kit	Qiagen	Cat#: 74104
RNase-Free DNase Set	Qiagen	Cat#: 79254
TransIT-LT1 Transfection Reagent	Mirus	Cat#: MIR 2300
Deposited Data		
Raw and analyzed data	This paper	GEO:GSE158786
Experimental Models: Cell Lines		
keratinocytes	This paper	N/A
Skin explants	This paper	N/A
Experimental Models: Organisms/Strains		
Mouse: K10-rtTA	(Muroyama and Lechler, 2017)	N/A
Mouse: TRE-Spastin	(Muroyama and Lechler, 2017)	N/A
Mouse: Involucrin-tTA	(Jaubert et al., 2004)	N/A
Mouse: TRE-Arhgef11^{CA}	This paper	N/A
Mouse: TRE-H2BGFP	Jackson Laboratories	Stock#: 005104
Mouse: Rosa-mT/mG	Jackson Laboratories	Stock#: 007576
Mouse: CMV-Cre	Jackson Laboratories	Stock#: 006054
Mouse: mGFP	This paper	N/A
Mouse: Tyr-Cre	Jackson Laboratories	Stock#: 029788
Mouse: Krt14Cre	Jackson Laboratories	Stock#: 018964
Mouse: Rosa26-LSL-H2B mCherry	Jackson Laboratories	Stock#: 023139
Mouse: E-cadherin-mCFP	Jackson Laboratories	Stock#: 016933
Mouse: CD1 IGS	Charles River	Strain code: 022
Oligonucleotides - See Table 1		
Recombinant DNA		
Plasmid: pTRE2-HA-Arhgef11^{CA}	This paper	N/A
Plasmid: K14-rtTA	This paper	N/A
Software and Algorithms		
Fiji software		https://imagej.net/Fiji
GSEA software	(Subramanian et al., 2005)	https://www.gsea-msigdb.org/gsea/index.jsp
WebGestalt	(Wang et al., 2017)	http://www.webgestalt.org/
Prism 8	GraphPad	8.3.0

REAGENT or RESOURCE	SOURCE	IDENTIFIER
Microsoft Excel	Microsoft	2016
Other		
Sterile Celltrics 30 μm filters	Sysmex	Cat#: 04-004-2326
Lumox dish 35	Sarstedt	Cat#: 94.6077.331

Table 1 -

Oligonucleotides Used

	Source	Identifier
K10-rtTA_genotyping_Forward: CCATTCTCAGTTTCAACATAGC	(Muroyama and Lechler, 2017)	N/A
K10-rtTA_genotyping_Reverse: CCTTGTCGTCAGGCCTTCG	(Muroyama and Lechler, 2017)	N/A
TRE-Spastin_genotyping_Forward: CCATACGATGTTCCAGATTACG	(Muroyama and Lechler, 2017)	N/A
TRE-Spastin_genotyping_Reverse: CGAGGCAATGAATTACTAGC	(Muroyama and Lechler, 2017)	N/A
Involucrin-tTA_genotyping_Forward: AGGGAAGAGGGGATGCTAAA	(Jaubert et al., 2004)	N/A
Involucrin-tTA_genotyping_Reverse: CCATCGCGATGACTTAGT	(Jaubert et al., 2004)	N/A
TRE-Arhgef11^{CA}_genotyping_Forward: CGTCGCCTTCCACGAACGG	This paper	N/A
TRE-Arhgef11^{CA}_genotyping_Reverse: CTCTCCTTGCGTTGTTTAGTCC	This paper	N/A
TREH2BGFP_genotyping	Jackson Laboratories	11029, 40383
Rosa-mT/mG_genotyping	Jackson Laboratories	17062, 24500, 36158
CMV-Cre_genotyping	Jackson Laboratories	oIMR1084, oIMR1085
Tyr-Cre_genotyping	Jackson Laboratories	14314, 38998
Krt14Cre_genotyping	Jackson Laboratories	oIMR1084, oIMR1085
Rosa26-LSL-H2B mCherry_genotyping	Jackson Laboratories	10507, oIMR8545, oIMR8546
E-cadherin-mCFP_genotyping	Jackson Laboratories	12772, 12773, 12774